Helicase-mediated mechanism of SSU processome maturation and disassembly

Olga Buzovetsky[1] and Sebastian Klinge[1,*]

1 Laboratory of Protein and Nucleic Acid Chemistry, The Rockefeller University, New York, New York 10065, USA

*Correspondence: klinge@rockefeller.edu (S.K.)

ABSTRACT

Eukaryotic ribosomal small subunit (SSU) assembly requires the SSU processome, a nucleolar precursor containing the RNA chaperone U3 snoRNA. The underlying molecular mechanisms of SSU processome maturation, remodeling, disassembly, RNA quality control, and the transitions between states remain elusive due to a paucity of intermediates. Here we report 16 native SSU processome structures alongside genetic data, revealing how two helicases, the Mtr4-exosome and Dhr1, are controlled for accurate and unidirectional ribosome biogenesis. Our data show how irreversible pre-ribosomal RNA degradation by the redundantly tethered RNA exosome couples the transformation of the SSU processome into a pre-40*S* particle during which Utp14 can probe evolving surfaces, ultimately positioning and activating Dhr1 to unwind the U3 snoRNA and initiate nucleolar pre-40*S* release. This study highlights a paradigm for large dynamic RNA-protein complexes where irreversible RNA degradation drives compositional changes and communicates these changes to govern enzyme activity while maintaining overall quality control.

47

48 **MAIN**

49 The nucleolus, a membrane-less organelle, is generated via eukaryotic ribosome
50 biogenesis in a transcription-dependent manner. The maturation of ribosomal small
51 subunit (SSU) and large subunit (LSU) precursors generates distinct phases of this multi-
52 layered organelle, which is maintained via multi-valent RNA-protein and protein-protein
53 interactions. Early stages of eukaryotic ribosomal small subunit (SSU/40*S*) assembly
54 involve the SSU processome, a giant nucleolar particle containing approximately a
55 quarter of all eukaryotic ribosome assembly factors and three RNAs (SSU pre-rRNA/18*S*,
56 5′ ETS and the RNA chaperone U3 snoRNA)[1–3]. The 18*S* is composed of four domains
57 (5′, central, 3′ major, and 3′ minor) which are housed in separate modules. By serving as
58 the architectural blueprint for the SSU processome, the chaperone U3 snoRNA base-
59 pairs with parts of the SSU pre-rRNA as well as the 5′ ETS. High-resolution structural
60 studies of SSU processome assembly and maturation in yeast and human cells have
61 started to reveal isolated native states before and after cleavage of the mature rRNA 5′
62 end (site A1) [4–13]. After a poorly characterized departure of most assembly factors (SSU
63 processome disassembly) a pre-40*S* particle emerges, which in addition to compacted
64 rRNA domains still contains U3 snoRNA and the RNA helicase Dhr1[ref9] . The current
65 absence of intermediate states highlights our limited understanding of the mechanisms
66 that guide transitions between visualized states. The transition of the SSU processome
67 from maturation to disassembly was suggested to involve the RNA exosome (with
68 associated exonuclease Rrp6 and RNA helicase Mtr4)[10,12–15]. As the arbiter of RNA
69 quality control, the RNA exosome ensures correct RNA processing. This system requires

70 synergistic interactions between the RNA exosome and its substrates for RNA
71 surveillance. Substrates that remain tethered to the RNA exosome are subject to RNA
72 turnover whereas correctly processed RNA substrates are released[16]. The limited number
73 of visualized SSU processome maturation and disassembly states has prevented a
74 mechanistic understanding of their interaction with the RNA exosome and how RNA
75 exosome function is coupled to SSU processome maturation and disassembly.
76 Specifically, the mechanisms of RNA exosome recruitment, substrate access, and
77 disengagement remain unclear[12,13].

78 At the end of SSU processome disassembly, the DEAH-box helicase Dhr1 (DHX37
79 in humans) plays a key role in the removal of U3 snoRNA from a pre-40*S* particle to
80 facilitate the formation of the central pseudoknot. However, despite ample studies[17–21],
81 the mechanism with which Dhr1 is initially recruited to the SSU processome, kept in an
82 inactive conformation, subsequently repositioned to engage its substrate U3 snoRNA,
83 and ultimately activated, remains unknown. Presently there is a lack of understanding of
84 how the SSU processome, the RNA exosome, and Dhr1 work in concert to bring about
85 unidirectional maturation and disassembly while maintaining RNA quality control
86 throughout the entire process, which enables completed particles to leave from the
87 nucleolus.

88 To address this, we determined native high-resolution structures of 16
89 *Saccharomyces cerevisiae* SSU processome states undergoing maturation and
90 disassembly with resolutions up to 2.7 Ångstroms. Together with complementary genetics
91 and an *in silico* protein-protein interaction screen, we have elucidated an RNA exosome-
92 mediated mechanism that explains both SSU processome maturation and disassembly

93 as a function of the 3′ to 5′ helicase activity of the RNA exosome-bound helicase Mtr4.
94 Within this framework SSU processome disassembly, exosome-mediated RNA
95 surveillance, and Dhr1 activation are tightly coordinated to maintain RNA quality control
96 during the entire pathway.

97 To determine how Dhr1-bound SSU processomes undergo maturation and
98 disassembly, we obtained native cryo-EM structures of particles containing Dhr1 during
99 early, intermediate, and late stages (**Fig. 1 and Extended Data Fig. 1**). Early assembly
100 states were selected using Dhr1 and the early assembly factor Kre33 as affinity baits
101 (Dataset 1, **Supplementary Fig. 1**). For unbiased views of all Dhr1-bound states, Dhr1
102 was used as the sole affinity bait (Dataset 2, **Supplementary Fig. 2**). The late
103 disassembly state containing activated Dhr1 (here State O) was obtained by selecting for
104 particles containing Dhr1 and its activator Utp14 and lacking Utp7, which is present in
105 earlier intermediates (Dataset 3, **Supplementary Fig. 3**).

106 From a total of 213,766 cryo-EM images, initial data curation and comprehensive
107 3D classifications yielded 16 SSU processome reconstructions (states A-O) with overall
108 resolutions of 2.7-6 Ångstroms (**Fig. 1 and Extended Fig. 1**). Focused refinements with
109 105 maps were used to obtain 16 composite maps for all structures (**Supplementary**
110 **Figs. 4-25**), which enabled model building and assignment of 50 unique assembly factors,
111 21 ribosomal proteins, and three RNAs (5′ ETS, 18S rRNA, and U3 snoRNA) across all
112 states (**Extended Data Table 1**). Here, states are defined based on distinct rRNA folding
113 transitions and the presence or absence of distinct assembly factors resulting in 15 unique
114 states (States A-O), and a substate of State A that undergoes conformational changes
115 only (State A*). Together these states provide unprecedented high-resolution coverage

116 of native SSU processome maturation and disassembly that goes far beyond prior
117 studies[9,10,12] (**Extended Data Fig. 1-6, Supplementary Fig. 26 and 27**).
118
119 **Chronology of SSU biogenesis**
120 The large number of observed states allows us to visualize nucleolar SSU biogenesis as
121 a function of RNA exosome-mediated 5′ ETS degradation, which first triggers cleavage
122 of the 18*S* rRNA at site A1 (States A-G), and subsequently orchestrates SSU processome
123 disassembly, rRNA compaction, and activation of Dhr1 (States H-O) (**Fig. 1, Extended**
124 **Data Fig. 1 and 2**). This is contrary to prior studies which lacked the temporal resolution
125 to precisely define both the chronology and causality of events leading to cleavage at site
126 A1 and hence the underlying mechanism (**Supplementary Fig. 26**)[9]. Initial degradation
127 of the 3′ end of the 5′ ETS on the exterior of the particle is followed by accommodation of
128 the C-terminus of Rrp6 (State C), suggesting that the RNA exosome is responsible for
129 this remodeling step. In State D the restructuring of the 5′ ETS in the interior of the SSU
130 processome allows for partial release of Krr1 and Faf1 from their binding sites. This leads
131 to the 3′ end of the 18*S* rRNA precursor (helix 45) to be chaperoned by the assembly
132 factor Pno1 towards the interior of the particle, thus allowing an N-terminal element of the
133 DEAH-box helicase Dhr1 to bind. As the assembly factor Utp14 connects Pno1 with Dhr1
134 (**Supplementary Fig. 27 e and i**), the integration of helix 45 near the central domain
135 results in the docking of the auto-inhibited Dhr1 in State E. Surprisingly we find that A1
136 cleavage in State G is solely triggered by the incorporation of Dim1 as this protein couples
137 the interrogation of helix 45 installation with the stabilization of U3 snoRNA-bound regions
138 within the 18S rRNA in an upward conformation. This facilitates Utp24-mediated A1

139 cleavage in particles that still contain the Kre33 module, which was previously thought to
140 precede A1 cleavage[9] (**Fig. 1, Extended Data Fig. 3**).

141 SSU processome disassembly further progresses as a function of 3′ to 5′
142 elimination of the 5′ ETS, resulting in compositional and conformational changes of the
143 particle (**Fig.1**). During these compositional changes, Utp14, a largely unstructured
144 protein containing several regulatory segments visualized in our structures (here referred
145 to as a-f) can adopt different binding conformations as a response to SSU processome
146 maturation and disassembly (**Extended Data Fig.6 a,d,e**).

147 With the processing of the 5′ hinge, distinct stages of disassembly are observed
148 that involve the stepwise departure of assembly factors, such as Rrp5, Sof1, and Utp7
149 (States H-J). In States J and K, Utp14 licenses a new binding site for Dhr1, which was
150 previously occupied by Utp7. The subsequent processing of the 3′ hinge (States K-L)
151 releases much of the UtpB complex (except for Utp18) and the helicase Dhr1. In a major
152 compositional remodeling step, the transition from State L to M marks the complete
153 elimination of the 5′ ETS, which triggers the departure of the UtpA and UtpB complexes
154 as well as individual assembly factors and Rrp6. This remodeling step subsequently
155 allows Dhr1 to be repositioned and activated by Utp14 in a state-specific manner. States
156 M-O therefore capture the activation of Dhr1 as further compaction of the particle triggers
157 the undocking of U3 snoRNP proteins and Utp20. These results suggest a direct
158 mechanism by which the RNA exosome could degrade the 5′ ETS to trigger large
159 compositional and conformational changes that transform the SSU processome into a
160 pre-40*S* particle.

161

162 **Integrated nucleolar RNA surveillance**

163 Genetic studies suggested that the yeast RNA exosome binds the SSU processome via
164 an interaction between the RNA helicase Mtr4 arch domain and the assembly factor
165 Utp18 via an arch-interacting motif (AIM)[14] . While low-resolution density for the RNA
166 exosome in the proximity of the SSU processome has been observed[10,12], exactly how
167 exosome recruitment and positioning is achieved across multiple states remains unclear.
168 Moreover, the RNA exosome must efficiently detect and eliminate trapped SSU
169 precursors within the nucleolus which have failed to complete biogenesis, yet how
170 nucleolar RNA surveillance is set up to do so remains unresolved[10,12,14] . The 71 proteins
171 present in the SSU processome together with the 14 proteins present within the RNA
172 exosome provide a unique opportunity to screen pathway-wide protein-protein
173 interactions *in silico* using Alphafold-Multimer[22–24]. We employed this approach to obtain
174 an SSU processome predictome to test 3,570 unique binary interactions, which together
175 with our high-resolution cryo-EM maps enabled the identification of many previously
176 unknown interactions (**Fig. 2a, Extended Data Fig. 4, and Extended Data Table 2**).
177 These data highlight key features of the SSU biogenesis pathway including the
178 architectural roles of Sas10-domain containing complexes, tethering functions of Mpp10
179 for ribosomal protein S5 and Dim1, and predictions for the recruitment and activation of
180 Dhr1/DHX37 (**Extended Data Fig. 4d,f**). In addition, mutually exclusive interactions
181 between Kre33 and Faf1 or Bms1 are revealed, which now explain previously unassigned
182 density for the human homologs of Kre33/Faf1 (NAT10/C1ORF13) in the human SSU
183 processome[11] (**Extended Data Fig. 4e**).

184 A striking series of predicted interactions emerged from the SSU processome
185 predictome that suggest extensive contacts between the RNA degradation machinery and
186 the maturing and disassembling SSU processome **(Fig. 2a,b**). In addition to previously
187 known interactions between the RNA helicase Mtr4 and Utp18[ref14] and newly identified
188 multivalent interactions between the yeast Rrp6 C-terminus (lasso) and the SSU
189 processome in this study, the SSU processome predictome suggested that Utp14, the
190 essential activator of Dhr1, additionally serves as a bridge between Mtr4 (via Exosome
191 Recruitment Motif 1, ERM1), the core exosome component Rrp40 (via ERM2), and the
192 SSU processome (**Fig. 2a,b**). This mode of binding is similar to the binding of the RNA
193 exosome cofactor Mpp6[ref25], with Mpp6 motifs having a high degree of sequence similarity
194 to Utp14 ERM1 and ERM2 (**Extended Data Fig. 5a**).

195 Based on these predictions, a model emerges in which the RNA exosome contains
196 four contact points for the SSU processome, which in addition to Utp18 AIM and the C-
197 terminus of Rrp6 (lasso) include two peptides of Utp14 (ERM1 and ERM2) (**Fig. 2b**).
198 Synergistically, the 2.7 Ångstrom structure of State H highlights that elements of Rrp6,
199 Utp18 (AIM), and predicted Utp14 (ERM1 and ERM2) are all positioned in close proximity
200 to the 3′ end of the 5′ ETS where the Mtr4 helicase needs to unwind the 5′ETS for both
201 maturation and disassembly to occur (**Fig. 2c**). In State H, Utp14 occupies a strategic
202 position with key regulatory elements that respond to conformational changes of the entire
203 particle. Elements of Utp14 that will in later states provide a part of a Dhr1 binding site
204 (segment b) or activate Dhr1 (segments d and e) are sequestered in State H near
205 Sof1/Utp20 and Utp7/Utp1 respectively (**Fig. 2c,d).** Separately, the newly identified Utp14
206 hook (segment c) recruits the auto-inhibited Dhr1 and this inactive state is further

207 stabilized by N-terminal elements of Pno1 (**Supplementary Fig. 27i,l**). This arrangement
208 places ERM1 and ERM2 of Utp14 directly between segments b and c so that after
209 cleavage at site A1 all elements that bridge the SSU processome and the RNA exosome
210 are present near the 3′ end of the 5′ ETS (**Fig. 2c,d**).

211 The network consisting of Utp18, Rrp6 and Utp14 suggests that beyond exosome
212 catalytic function, connective redundancy may play a major role in ensuring correct
213 placement of the RNA exosome near the SSU processome. While prior data have
214 indicated that Utp18 AIM mutants are synthetically lethal in the absence of Rrp6[ref12,14],
215 the relative contributions of Rrp6 exonuclease activity and its ability to bind to the SSU
216 processome have remained unclear. Using yeast genetics we show that in the absence
217 of the Utp18 AIM, an inactive Rrp6 exonuclease (Y361A)[26] results in synthetic lethality,
218 suggesting that catalytic activity of Rrp6 becomes essential if Mtr4 helicase cannot be
219 correctly positioned (**Fig. 2e**). These data suggest that both positioning and the
220 redundancy in connections of the RNA exosome to the SSU processome is essential for
221 its function. Without the Utp18 AIM, three connections to the SSU processome remain
222 via the Rrp6 lasso and the predicted Utp14 ERM1 & ERM2 (**Fig. 2a**). Our genetic data
223 indicate that as long as any one of these connections is present, cell viability is
224 maintained. By contrast, synthetic lethality is observed if all four connections are disrupted
225 (**Fig. 2e**). Since the Rrp6 lasso is a multivalent binder of the SSU processome with four
226 binding sites, we could separately show that iterative Rrp6 C-terminal truncations in a
227 genetic background lacking the Utp18 and Utp14 connections gradually reduce growth
228 (**Extended Data Fig. 5**). The SSU processome predictome together with structural data
229 and genetics reveal a highly redundant nucleolar tethering network that couples SSU

processome maturation, disassembly and RNA quality control. These findings are further consistent with the visualization of the human homolog of Rrp6 (EXOSC10) in the immediate vicinity of nucleolar SSU precursors[27] .

Synchronized exosome-mediated disassembly

Elucidating the precise molecular mechanisms governing the controlled disassembly of the SSU processome remains a significant challenge, as current models lack the necessary sampling and resolution to mechanistically explain this process[9]. Here, States H-O capture a series of intermediates that follow RNA exosome-mediated disassembly (**Figs. 1 and 3**), allowing us to mechanistically explain how disassembly and RNA quality control are coupled. The irreversible 3′ to 5′ elimination of the 5′ ETS by the RNA exosome is directly coupled to the release of assembly factors in the exosome's path. These include, among others, the Sof1-Utp7 complex at the 5′ hinge, the UtpB complex at the 3′ hinge, and finally Utp18 and the UtpA complex positioned at the start of the 5′ ETS (**Fig. 3a**). RNA exosome-mediated compositional changes to the SSU processome result in three key events that occur concurrently. First, the reduction of multi-valent RNA-protein and protein-protein interactions within the SSU processome leads to release of bound and tethered complexes. Second, the RNA exosome loses two of its interaction sites with the SSU processome and its function transitions from substrate engagement to substrate monitoring. Third, the changes of the SSU processome landscape provide new binding surfaces for Utp14, which organizes both Dhr1 repositioning and activation (**Fig. 3**).

252 Beginning in State H, RNA exosome mediated processing of the 3′ end of the 5′
253 ETS alters the Sof1 binding site, weakening its interaction with Utp7 until only the C-
254 terminus of Utp7 remains bound in State I. During this transition, key regulatory elements
255 of Utp14 involved in subsequent Dhr1 recruitment (segment b) and activation (segments
256 d and e) are released while remaining tethered via peptides bound to Dhr1 and Pno1
257 (segments c and f respectively). During subsequent 5′ ETS degradation, represented in
258 states J and K, the Utp7 C-terminus is released, and its binding site is gradually occupied
259 by elements of Utp14 (segments a and b) that prepare a binding site for Dhr1 as the UtpC
260 complex is released. During the transition from State K to L, continued 5′ ETS processing
261 results in UtpB losing its primary binding site at the 3′ hinge while remaining tethered to
262 the SSU processome via Utp18, and Dhr1 remains connected to the particle via its N-
263 terminus and the Utp14 hook (segment c) (**Fig. 3b**). Following complete 5′ ETS removal
264 during the transition from State L to State M, UtpA, associated proteins, Utp18, and Rrp6
265 are fully released (**Fig. 3, Extended Data Fig. 6a**). During this key transition the roles of
266 the RNA exosome and Dhr1 are dramatically changed.

267 The role of the RNA exosome shifts from the active substrate engaged state with
268 four binding sites on the SSU processome to an overall surveillance state through the
269 remaining two Utp14 ERM sites (**Extended Data Fig. 6a**). Furthermore, re-engagement
270 of the substrate by the RNA exosome is prevented by the lack of a Utp18 binding site and
271 the occlusion of the Rrp6 lasso binding site by the C-terminus of ribosomal protein S4
272 (**Fig. 3b, Extended Data Fig. 6b and c**). Separately, the role of Dhr1 changes from a
273 tethered auto-inhibited state to a repositioned, substrate engaged, and activated enzyme
274 poised to remove U3 snoRNA from the pre-40*S* particle.

275 **Molecular circuitry of Dhr1 activation**

276 High-resolution crystal structures of Dhr1/DHX37 have shown that this DEAH-box
277 helicase in isolation can exist in two states, an inactive state in which an auto-inhibitory
278 loop prevents substrate binding, and an active state, in which single-stranded RNA acts
279 as a substrate[11,19]. However, thus far no Utp14-mediated active state of Dhr1 has been
280 observed. The comparison between the inactive state of Dhr1 in State H and the Utp14-
281 mediated active state of Dhr1 in State O now rationalizes how irreversible RNA exosome-
282 mediated 5′ ETS degradation orchestrates a cascade of events that triggers Dhr1
283 activation in a state-specific manner during SSU processome disassembly (**Fig. 4**).

284 In State H, the UtpB tetramer provides binding sites for both Dhr1 and Pno1
285 (elements 1 and 4), which enable additional elements of Pno1 (elements 2 and 3) to
286 stabilize the auto-inhibited state of Dhr1. Element 3 of Pno1 stabilizes the auto-inhibitory
287 loop of Dhr1, while element 2 of Pno1 prevents binding of segment d of Utp14, thus
288 preventing a switch towards Dhr1 activation (**Fig. 4a**). Separately, segments of Utp14 that
289 subsequently provide a binding site (segment b) or activate Dhr1 (segments d and e) are
290 sequestered by Utp20/Sof1 and Utp7-Utp1 respectively (**Figs. 2c, 4a, c**).

291 In State O, the prior RNA exosome-mediated elimination of the UtpB complex, and
292 the release of Utp14 segments a-e have dramatically changed the local environment for
293 Dhr1. The new Dhr1 binding site (Utp14 segments a and b) is formed on top of its
294 substrate U3 snoRNA, which still base-pairs with 18*S* elements that will form the central
295 pseudoknot upon Dhr1-mediated U3 snoRNA release (**Fig. 4b**). The relative positions of
296 Utp14 elements c and f now enable Utp14 elements d and e to stabilize a conformation
297 of Dhr1 in which the RecA lobes are dramatically shifted to engage the substrate U3

298 snoRNA while displacing the auto-inhibitory loop (**Fig. 4b, d**). The architecture of the
299 Utp14-mediated active form of Dhr1 in State O rationalizes a wealth of genetic and
300 biochemical data from yeast and mammalian systems, highlighting that this mode of
301 activation is distinct from G-patch mediated DEAH-box helicase activation (**Extended**
302 **Data Fig. 6e-g**)[19,21].

303 Thus, RNA exosome-mediated remodeling of the SSU processome triggers a
304 series of compositional and conformational changes within the disassembling SSU
305 processome that collectively switch Dhr1 from an "OFF" into an "ON" state that enables
306 its engagement and processing of U3 snoRNA. The irreversible release of U3 snoRNA
307 and the formation of the central pseudoknot prepare the resulting pre-40*S* particle for
308 subsequent nuclear maturation where Utp14 is replaced by Nob1[ref2], releasing the final
309 link to nucleolar RNA surveillance.

310

311 **Conclusions**

312 Nuclear bodies that contain biosynthetic processing pathways such as the nucleolus,
313 Cajal bodies, and nuclear speckles share unified organizational principles by which RNA
314 synthesis and processing results in the formation and dynamics of these multi-valent
315 condensates[28,29]. For nucleolar SSU processome maturation and disassembly, we
316 present a high-resolution temporal perspective, highlighting that this highly dynamic
317 process is driven by the activities of two RNA helicases associated with the RNA
318 degradation machinery (Mtr4) and the SSU processome itself (Dhr1) (**Figs. 1 and 2**). The
319 irreversible unwinding and degradation of pre-ribosomal RNA (5′ ETS) changes the
320 composition of disassembling SSU processomes, allowing regulatory peptides of Utp14

321 to probe the changing landscape of these particles to state-specifically reposition and
322 activate Dhr1 for the terminal and irreversible release of U3 snoRNA (**Figs. 3 and 4**). The
323 emerging model now highlights the importance of multivalent tethering at three levels.
324 First, intra-SSU processome tethering enables pre-recruitment of assembly factors
325 required for subsequent steps including restructuring of the SSU processome and A1
326 cleavage. Second, the extent (valency) of tethering between large particles such as the
327 RNA exosome to the SSU processome changes as the exosome matures and
328 disassembles the SSU processome, thereby shifting the role of the RNA exosome from
329 initial recognition to substrate engagement and finally substrate surveillance. Third, at the
330 level of the organelle, overall tethering of the maturing and disassembling SSU
331 processomes to the nucleolus is decreased as more and more nucleolar assembly factors
332 are released, thereby reducing the overall valency of particles before nucleolar release
333 (**Fig. 5**). The scope of our study now allows us to illustrate molecular events at the
334 Ångstrom scale that can rationalize the organizational principles at the micrometer scale
335 as observed for the nucleolus[27]. This study highlights molecular transitions in large
336 dynamic RNA-protein complexes driven by RNA helicases, and how these changes may
337 be coupled to movement through biomolecular condensates in nuclear bodies.
338
339
340
341
342
343

REFERENCES

1. Dragon, F. *et al.* A large nucleolar U3 ribonucleoprotein required for 18S ribosomal RNA biogenesis. *Nature* **417**, 967–970 (2002).

2. Dörner, K., Ruggeri, C., Zemp, I. & Kutay, U. Ribosome biogenesis factors—from names to functions. *Embo J* e112699 (2023) doi:10.15252/embj.2022112699.

3. Broeck, A., Vanden & Klinge, S. Eukaryotic Ribosome Assembly. *Annual Review of Biochemistry* **Volume 93 (In press)**, (2024).

4. Kornprobst, M. *et al.* Architecture of the 90S Pre-ribosome: A Structural View on the Birth of the Eukaryotic Ribosome. *Cell* **166**, 380–393 (2016).

5. Chaker-Margot, M., Barandun, J., Hunziker, M. & Klinge, S. Architecture of the yeast small subunit processome. *Science* **355**, eaal1880 (2017).

6. Sun, Q. *et al.* Molecular architecture of the 90S small subunit pre-ribosome. *Elife* **6**, e22086 (2017).

7. Barandun, J. *et al.* The complete structure of the small-subunit processome. *Nat. Struct. Mol. Biol.* **24**, 944–953 (2017).

8. Cheng, J., Kellner, N., Berninghausen, O., Hurt, E. & Beckmann, R. 3.2-Å-resolution structure of the 90S preribosome before A1 pre-rRNA cleavage. *Nat. Struct. Mol. Biol.* **24**, 954–964 (2017).

9. Cheng, J. *et al.* 90S pre-ribosome transformation into the primordial 40S subunit. *Science* **369**, 1470–1476 (2020).

10. Du, Y. *et al.* Cryo-EM structure of 90S small ribosomal subunit precursors in transition states. *Science* **369**, 1477–1481 (2020).

11. Singh, S., Broeck, A. V., Miller, L., Chaker-Margot, M. & Klinge, S. Nucleolar maturation of the human small subunit processome. *Science* **373**, eabj5338 (2021).

12. Lau, B. *et al.* Structure of the Maturing 90S Pre-ribosome in Association with the RNA Exosome. *Mol. Cell* **81**, 293-303.e4 (2021).

13. Broeck, A. V. & Klinge, S. An emerging mechanism for the maturation of the Small Subunit Processome. *Current Opinion in Structural Biology* **73**, 102331 (2022).

14. Thoms, M. *et al.* The Exosome Is Recruited to RNA Substrates through Specific Adaptor Proteins. *Cell* **162**, 1029–1038 (2015).

375 15. Hunziker, M. *et al.* Conformational switches control early maturation of the
376 eukaryotic small ribosomal subunit. *Elife* **8**, 213 (2019).

377 16. Keidel, A., Long, C. L., Iwasa, J. & Conti, E. RNA-Degrading Exosome Complexes:
378 Molecular Mechanisms and Structural Insights. *Annu. Rev. Cell Dev. Biol.* (2025)
379 doi:10.1146/annurev-cellbio-111822-115115.

380 17. Sardana, R. *et al.* The DEAH-box helicase Dhr1 dissociates U3 from the pre-rRNA
381 to promote formation of the central pseudoknot. *PLoS Biol* **13**, e1002083 (2015).

382 18. Zhu, J., Liu, X., Anjos, M., Correll, C. C. & Johnson, A. W. Utp14 recruits and
383 activates the RNA helicase Dhr1 to undock U3 snoRNA from the pre-ribosome.
384 *Molecular and Cellular Biology* **36**, MCB.00773-15 (2016).

385 19. Boneberg, F. M. *et al.* Molecular mechanism of the RNA helicase DHX37 and its
386 activation by UTP14A in ribosome biogenesis. *RNA* **25**, 685–701 (2019).

387 20. Choudhury, P., Hackert, P., Memet, I., Sloan, K. E. & Bohnsack, M. T. The human
388 RNA helicase DHX37 is required for release of the U3 snoRNP from pre-ribosomal
389 particles. *RNA Biol* **16**, 54–68 (2018).

390 21. Lin, R., Elmir, E., Reynolds, M. J. & Johnson, A. W. In vitro characterization of the
391 yeast DEAH/RHA RNA helicase Dhr1. *J. Biol. Chem.* **301**, 108366 (2025).

392 22. Evans, R. *et al.* Protein complex prediction with AlphaFold-Multimer. *bioRxiv*
393 2021.10.04.463034 (2021) doi:10.1101/2021.10.04.463034.

394 23. Yu, D., Chojnowski, G., Rosenthal, M. & Kosinski, J. AlphaPulldown—a python
395 package for protein–protein interaction screens using AlphaFold-Multimer.
396 *Bioinformatics* **39**, btac749 (2022).

397 24. Schmid, E. W. & Walter, J. C. Predictomes, a classifier-curated database of
398 AlphaFold-modeled protein-protein interactions. *Mol. Cell* **85**, 1216-1232.e5 (2025).

399 25. Wasmuth, E. V., Zinder, J. C., Zattas, D., Das, M. & Lima, C. D. Structure and
400 reconstitution of yeast Mpp6-nuclear exosome complexes reveals that Mpp6 stimulates
401 RNA decay and recruits the Mtr4 helicase. *eLife* **6**, e29062 (2017).

402 26. Assenholt, J. *et al.* Exonucleolysis is required for nuclear mRNA quality control in
403 yeast THO mutants. *RNA (N. York, NY)* **14**, 2305–13 (2008).

404 27. Quinodoz, S. *et al.* Mapping and engineering RNA-controlled architecture of the
405 multiphase nucleolus. *bioRxiv* 2024.09.28.615444 (2024)
406 doi:10.1101/2024.09.28.615444.

407 28. Quinodoz, S. A. & Guttman, M. Essential Roles for RNA in Shaping Nuclear
408 Organization. *Cold Spring Harb. Perspect. Biol.* **14**, a039719 (2021).

409 29. Shan, L., Li, P., Yu, H. & Chen, L.-L. Emerging roles of nuclear bodies in genome
410 spatial organization. *Trends Cell Biol.* **34**, 595–605 (2024).

411 30. Mastronarde, D. N. Automated electron microscope tomography using robust
412 prediction of specimen movements. *J Struct Biol* **152**, 36–51 (2005).

413 31. Kimanius, D., Dong, L., Sharov, G., Nakane, T. & Scheres, S. H. W. New tools for
414 automated cryo-EM single-particle analysis in RELION-4.0. *Biochem J* **478**, 4169–4185
415 (2021).

416 32. Punjani, A., Rubinstein, J. L., Fleet, D. J. & Brubaker, M. A. cryoSPARC: algorithms
417 for rapid unsupervised cryo-EM structure determination. *Nat Methods* **14**, 290–296
418 (2017).

419 33. Zheng, S. Q. *et al.* MotionCor2: anisotropic correction of beam-induced motion for
420 improved cryo-electron microscopy. *Nat Methods* **14**, 331–332 (2017).

421 34. Zhang, K. Gctf: Real-time CTF determination and correction. *J Struct Biol* **193**, 1–12
422 (2016).

423 35. Asarnow, D., Cheng, D. A. E. P. Y. & Cheng, Y. UCSF pyem v0.5. Zenodo. (2019)
424 doi:10.5281/zenodo.3576630.

425 36. Punjani, A. & Fleet, D. J. 3D variability analysis: Resolving continuous flexibility and
426 discrete heterogeneity from single particle cryo-EM. *J. Struct. Biol.* **213**, 107702 (2021).

427 37. Wagner, T. *et al.* SPHIRE-crYOLO is a fast and accurate fully automated particle
428 picker for cryo-EM. *Commun Biol* **2**, 218–13 (2019).

429 38. Pettersen, E. F. *et al.* UCSF ChimeraX : Structure visualization for researchers,
430 educators, and developers. *Protein Sci* **30**, 70–82 (2020).

431 39. Jumper, J. *et al.* Highly accurate protein structure prediction with AlphaFold. *Nature*
432 **596**, 583–589 (2021).

433 40. Casañal, A., Lohkamp, B. & Emsley, P. Current Developments in Coot for
434 Macromolecular Model Building of Electron Cryo-microscopy and Crystallographic Data.
435 *Protein Sci.* pro.3791 (2019) doi:10.1002/pro.3791.

436 41. Afonine, P. V. *et al.* Real-space refinement in PHENIX for cryo-EM and
437 crystallography. *Acta Crystallogr D Struct Biol* **74**, 531–544 (2018).

438 42. Black, J. J., Sardana, R., Elmir, E. W. & Johnson, A. W. Bud23 promotes the final
439 disassembly of the small subunit Processome in Saccharomyces cerevisiae. *PLoS*
440 *Genet.* **16**, e1009215 (2020).

441

442

443

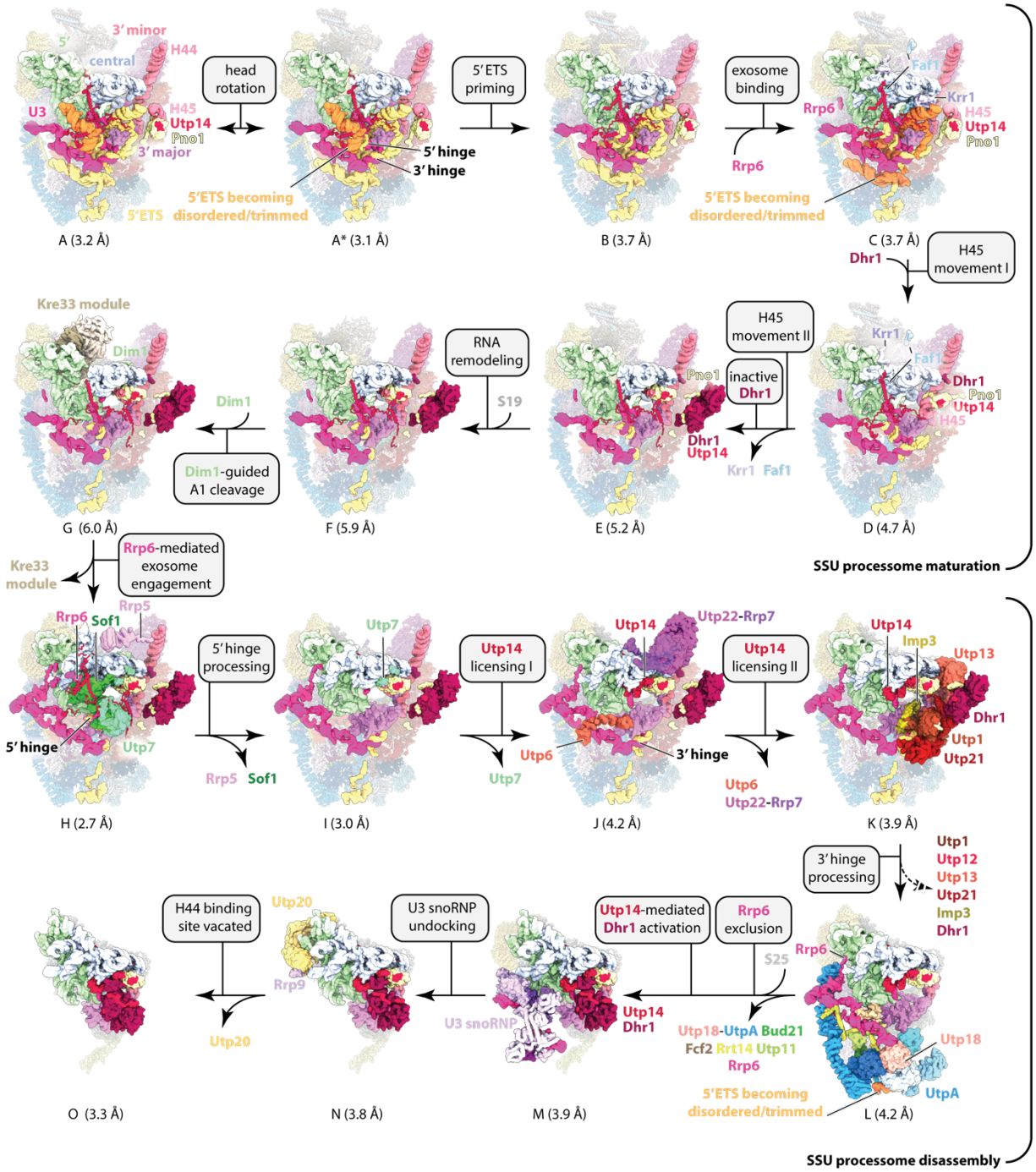

Fig. 1. SSU processome maturation and disassembly pathway.

Simplified atomic models of the SSU processome assembly pathway with color-coded rRNAs and ribosome assembly factors. Major changes in the rRNA between states are in the foreground and changes in protein compositions as well as functions are noted.

449 Elements of the 5′ ETS that will be removed are highlighted in orange. Proteins that
450 become ordered or depart between different assembly intermediates are indicated. The
451 overall resolution of each cryo-EM reconstruction is noted below each state. A dashed
452 arrow indicates tethering of protein components.
453
454
455
456
457
458
459

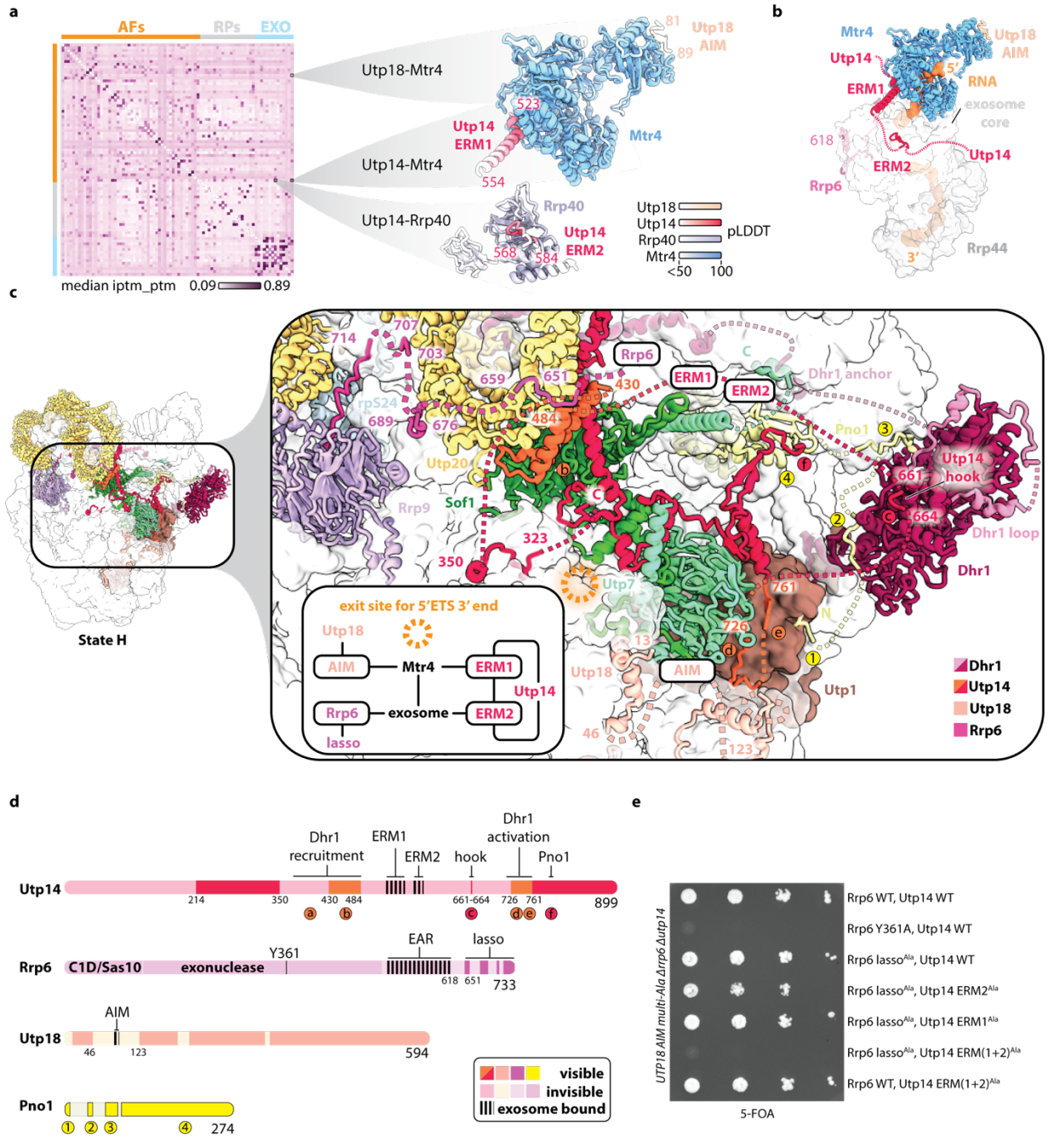

Fig. 2. Interaction networks between SSU processome and the RNA exosome.

(**a**) Yeast SSU processome predictome containing assembly factors (AFs), ribosomal proteins (RPs) and RNA exosome proteins (EXO) with color-coded confidence scores. Three AlphaFold-Multimer predictions are highlighted with color-coded proteins and

465 confidence levels (pLDDT). (**b**) AlphaFold predictions for color-coded Utp14, Mtr4, and
466 Utp18 AIM mapped onto a composite model of the RNA exosome with Rrp6 (PDBs 5vzj
467 and 6d6q). (**c**) Cartoon representation of state H (left) and zoomed-in view (right) of the
468 5′ ETS 3′ end exit site (orange circles) with color-coded exosome interacting proteins.
469 Regulatory elements of Utp14 are highlighted in orange. (**d**) Schematic of Utp14, Rrp6,
470 Utp18, and Pno1 protein sequences in State H with interacting and functional elements
471 labeled. (**e**) Growth analysis of Rrp6 and Utp14 mutants in a Utp18 multi-Ala background
472 on 5-FOA plates.
473
474

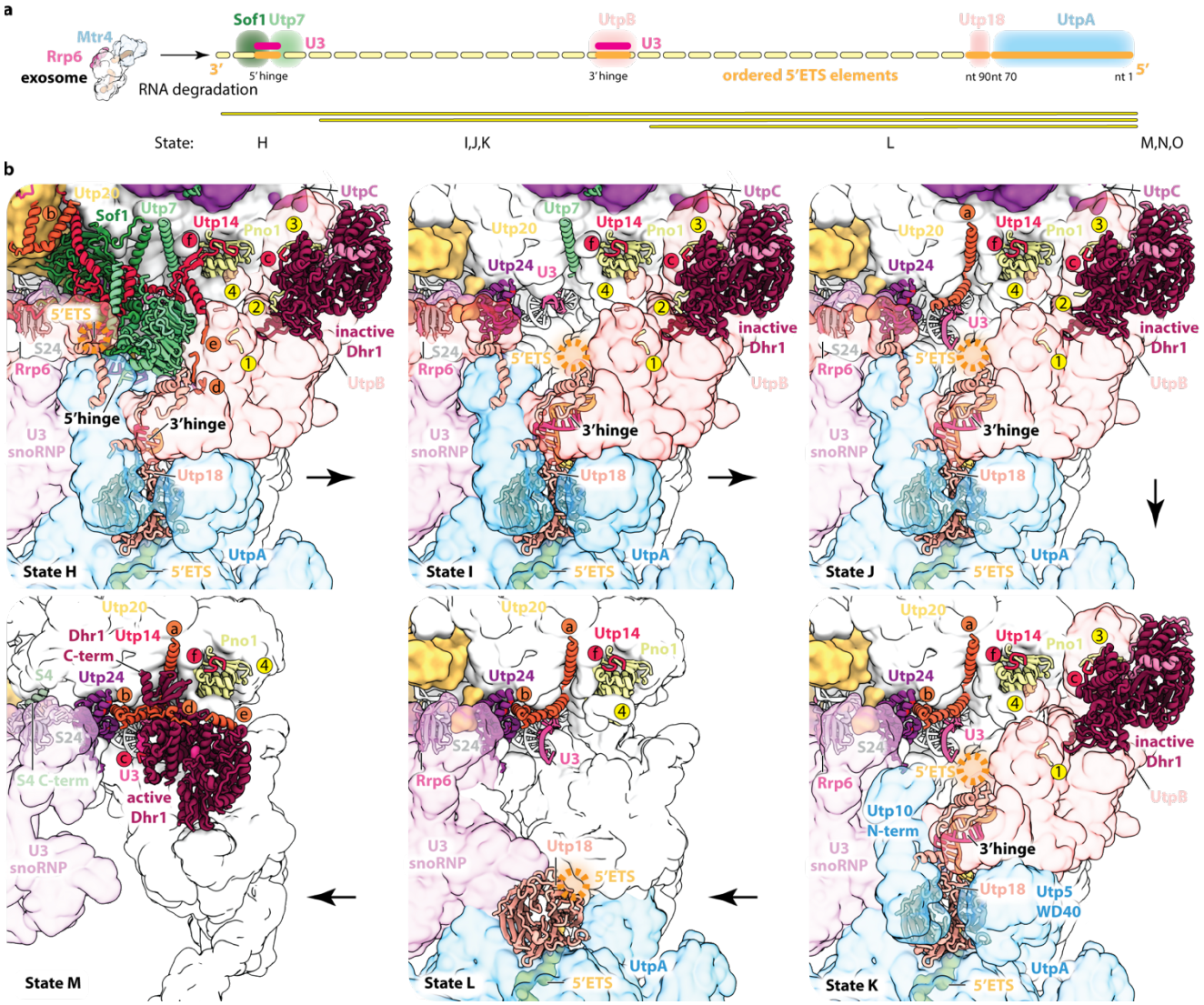

Fig. 3. Helicase-mediated disassembly is coupled to RNA quality control.

(**a**) Schematic of SSU processome disassembly as a function RNA degradation. RNA and protein elements bound to the 5′ ETS RNA are displayed as colored boxes and states with corresponding 5′ ETS length are listed below. (**b**) Architecture of the changes around the 5′ ETS exit sites (orange circles) from State H to M. Protein elements are color-coded and elements of Utp14 (b-f), Pno1 (1-4) and the state of Dhr1 are highlighted.

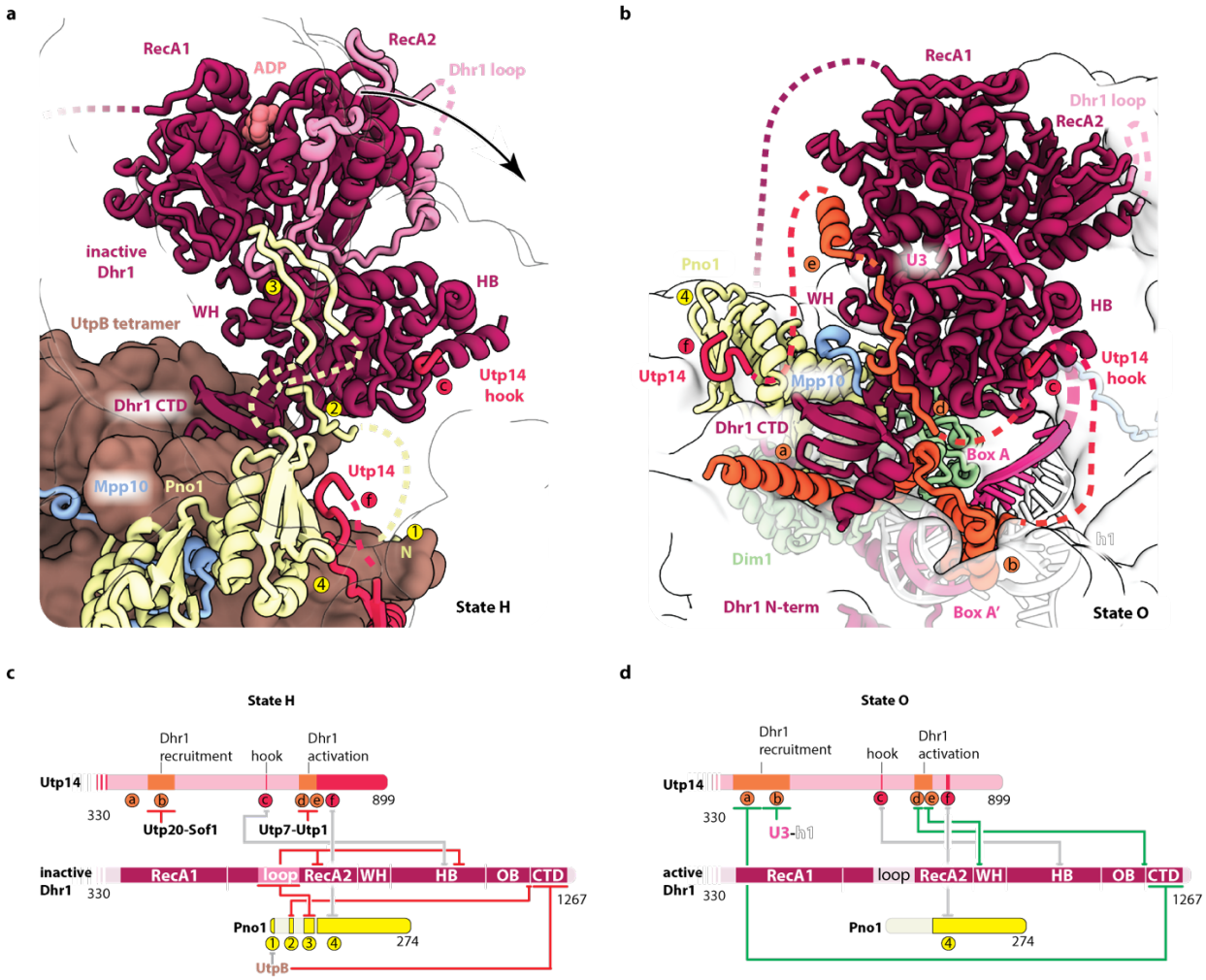

Fig. 4. Mechanism of Utp14-mediated Dhr1 activation.

(**a**) Zoomed-in view of inactive Dhr1 in State H, with auto-inhibitory loop (light pink) and inhibitory elements of Pno1 (1-4) and elements of Utp14 highlighted. The arrow indicates the conformational change of Dhr1 RecA domains. (**b**) Zoomed-in view of activated Dhr1 in State O. Activating Utp14 elements (a, b, d, and e) are highlighted in orange. (**c**) Schematic of State H molecular circuitry between Utp14, Dhr1 and Pno1. Interacting elements are colored grey and inhibitory interactions are indicated with red lines. (**d**) Schematic of State O molecular circuitry between Utp14, Dhr1 and Pno1. Interacting elements are colored grey and activating interactions are indicated with green lines.

494

495

496

497

498

499

500

501

502

503

504

505

506

507

508

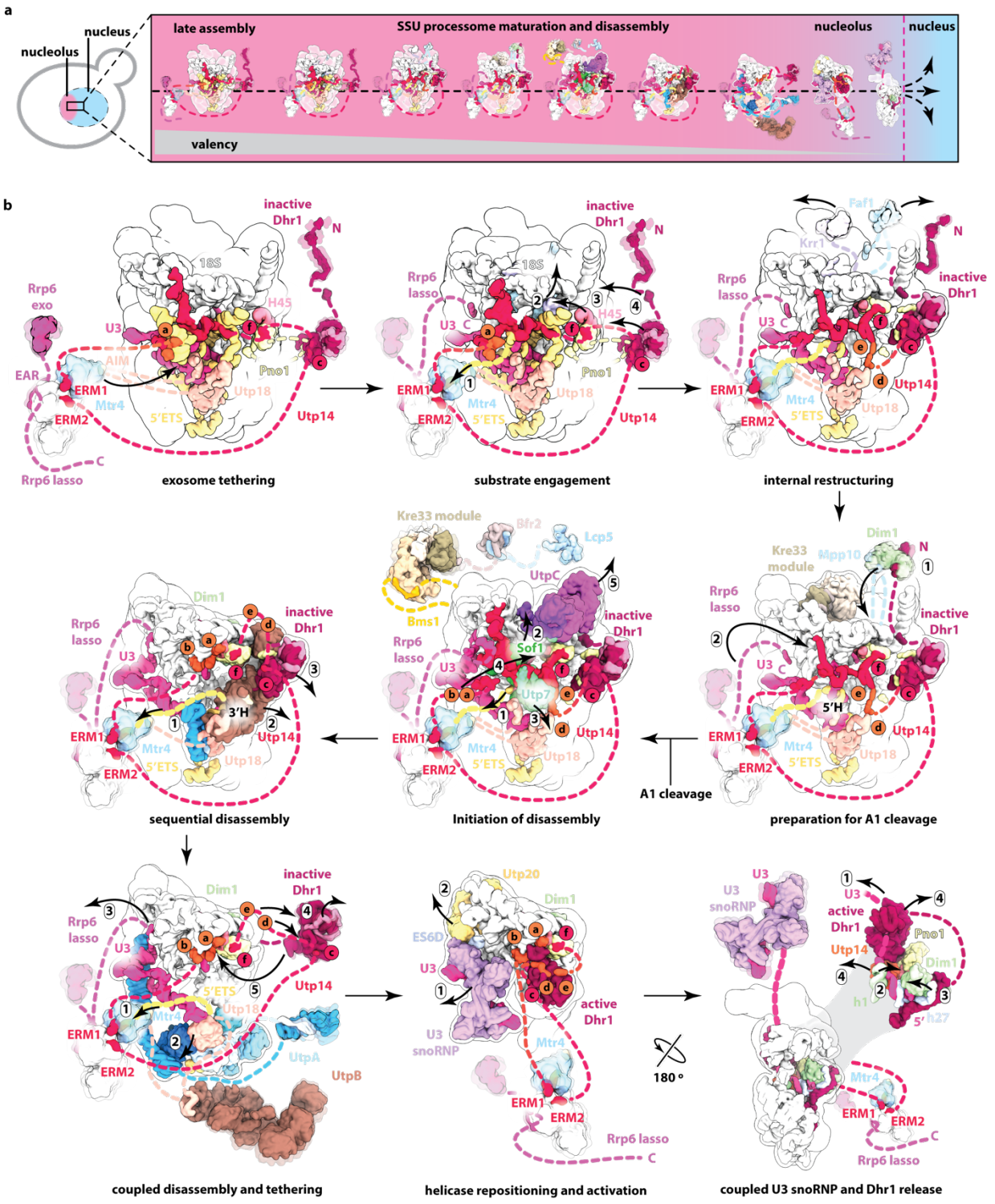

Fig. 5. Model of the mechanism of SSU biogenesis in the nucleolus.

(**a**) Schematic model of yeast SSU biogenesis in the nucleolus. Decreasing valency of maturing particles is indicated below. (**b**) SSU processome maturation and disassembly

513 pathway with key transitions are indicated. Color-coded tethered proteins and complexes
514 are indicated with linkers. Arrows and numbers highlight the order of transition steps (RNA
515 degradation, conformational changes, protein release, or protein repositioning to new
516 binding sites) that lead to particles with low valency during disassembly.
517
518
519
520
521
522
523
524
525
526
527
528
529
530
531
532
533
534
535

536 **METHODS**

537 **Generation of endogenously tagged DHR1, KRE33, UTP7 and UTP14 strains**

538 Assembly intermediates of the *S. cerevisiae* SSU processomes were purified from
539 three genetically modified BY4741 (MATa his3Δ leu2Δ0 met15Δ0 ura3Δ0) strains. Where
540 genes of interest (DHR1, KRE33, UTP7 and UTP14) were endogenously tagged: the first
541 strain containing C-terminal tandem 3C protease-cleavable mCherry and TEV-cleavable
542 alfa peptide tag on DHR1 along with a 3C cleavable C-terminal GFP-tag on KRE33 (MATa
543 his3Δ leu2Δ0 met15Δ0 ura3Δ0 DHR1-linker-tev-alfa tag-3c-mCherry under Hygromycin
544 B selection and KRE33-linker-tev-GFP under Nourseothricin selection), the second strain
545 containing only C-terminal tandem 3C protease-cleavable mCherry and TEV-cleavable
546 alfa peptide tag on DHR1 (MATa his3Δ leu2Δ0 met15Δ0 ura3Δ0 DHR1-linker-tev-alfa
547 tag-3c-mCherry under Hygromycin B selection) and the third strain containing C-terminal
548 tandem 3C protease-cleavable mCherry and a TEV-cleavable alfa peptide tag on DHR1
549 along with TEV cleavable C-terminal GFP-tag on UTP7 and C-terminally streptavidin-
550 binding-peptide (sbp) tag on UTP14 (MATa his3Δ leu2Δ0 met15Δ0 ura3Δ0 DHR1-linker-
551 tev-alfa tag-3c-mCherry under Hygromycin B selection and UTP7-linker-tev-GFP under
552 G418 selection and UTP14-linker-SBP under Nourseothricin selection). The three strains
553 were generated with standard genomic tagging techniques using the following primers for
554 yeast genomic tagging:

555 DHR1 forward primer:

556 TCACCAGAAAGGGCTTCCAGACCATCACAGGTGAAGAGAAAGAAAAAAAAACGCT
557 GCAGGTCGACGGATCC

558 DHR1 reverse primer:

559 TTAAGTGGTTGCAATTATTTGATGCCCTAGATAGGAATAATGTATTCTTCGGCAGAT

560 CCGCGGCCGCATAGG

561 Kre33 forward primer:

562 AAGAGATGAAAGCTATGAAAAAACCAAGAAAGTCTAAAAAGGCTGCAAATACGCTG

563 CAGGTCGACGGATCC

564 KRE33 reverse primer :

565 TGTAAAGGTTCAAACATCAACTATGTTTCTATTCTATATTATTGTACAAAGGCAGATC

566 CGCGGCCGCATAGG

567 UTP7 forward primer:

568 TTTCAGAAGACCACAAGGATGTCATCGAAGAGGCATTGAGCAGATTCGGCACGCT

569 GCAGGTCGACGGATCC

570 UTP7 reverse primer:

571 GCTATATTAATATGCAATCGATTCTCATACTGTCAACTTTTTGAACATGAGGCAGAT

572 CCGCGGCCGCATAGG

573 UTP14 forward primer:

574 TCATGACTAAGCCAGGCCAAGTTATTGATCCTTTGAAGGCACCATTTAAGACGCTG

575 CAGGTCGACGGATCC

576 UTP14 reverse primer:

577 ATTATTCCAGTATTACTATTCTACACAATGCATAATAAATAGATATAAAAGGCAGATC

578 CGCGGCCGCATAGG

579 The three strains were grown at 30 °C in YPD media (1% yeast extract, 2%

580 peptone and 2% glucose) to optical density of OD 1 measured at 600 nm. Cells were

581 harvested at 4,000*g* for 5 min, washed once with 1 l of ice cold ddH_2O and once with a

582 volume of ddH_2O supplemented with protease inhibitors (E64, pepstatin and PMSF) equal
583 to the mass of the cell pellet. The final pellets of ~30-40g were flash frozen in liquid
584 nitrogen. Pellets were lysed by cryo-grinding using a Retsch Planetary Ball Mill PM100
585 and powder was stored at –80 °C.
586
587 **Purification of SSU processome intermediates**
588 Cryo-ground powder was resuspended with buffer 1 (60mM Tris pH7.5, 50mM
589 NaCl, 2mM MgCl2, 5% glycerol, 0.1% NP-40) with addition of PMSF, pepstatin and E64
590 protease inhibitors. The suspension was cleared by centrifugation at 4 °C and 40,000*g*
591 for 20 min and lysate was incubated with 800 µl of packed NHS–sepharose beads
592 (Cytiva) coupled to anti-mCherry nanobodies for the first capture for all purifications and
593 incubated for 3.5 h at 4 °C on a nutator. Beads were pelleted by centrifugation at 4 °C for
594 1 min at 127*g*. After five washes in buffer 1, complexes were eluted in buffer EB (60mM
595 Tris, 50mM NaCl, 5mM MgCl2, 2% glycerol, 0.01% NP-40) supplemented with 3C
596 protease for 1 h at 4 °C. Beads were pelleted by centrifugation at 4 °C for 1 min at 127*g*
597 and supernatant was eluted and incubated with 80 µl of packed NHS–sepharose beads
598 (Cytiva) coupled to anti-GFP nanobodies for second capture (Dhr1/Kre33 and Dhr1/Utp14
599 purifications) while anti-alfa nanobodies were used for a second Dhr1 (Dhr1 only). Beads
600 were incubated for 1 h at 4 °C on a nutator and pelleted by centrifugation at 4 °C for 1 min
601 at 127*g* and washed twice with 2 ml of Buffer EB. After the second wash, for Dhr1/Kre33
602 and Dhr1 only purifications, beads were pelleted and resuspended with 25 µl of Buffer EB
603 supplemented with 1mM DTT and TEV protease and incubated on ice for 1 h. Beads
604 were pelleted by centrifugation at 4 °C for 10 min at 21,130g and the supernatant was

605 collected. For Dhr1/Utp14 purification, after the second capture (here Utp7), beads were
606 pelleted by centrifugation at 4 °C for 1 min at 127*g* and flowthrough was collected, the rest
607 of the beads were discarded (this step was used to remove earlier contaminating
608 complexes). The flowthrough was incubated with 40 µl of packed NHS–sepharose beads
609 (Cytiva) coupled to streptavidin for 1 h at 4 °C on a nutator. Beads were pelleted by
610 centrifugation at 4 °C for 1 min at 127*g* and washed twice with 2 ml of Buffer EB. After the
611 second wash, beads were pelleted and resuspended with 40 µl of Buffer EB
612 supplemented with 1mM DTT and 5 mM of D-biotin (Amresco) and incubated on ice for
613 20 min. Beads were pelleted by centrifugation at 4 °C for 10 min at 21,130g and the
614 supernatant was collected.
615
616 **Cryo-EM grid preparation and data acquisition**
617 Cryo-EM grids were prepared using a Vitrobot Mark IV robot (FEI Company) set
618 to 90% humidity and 18 °C temperature. Three and a half microliters of the eluted solution
619 was applied to a glow-discharged Quantifoil Au R3.5/1 with a layer of 2-nm ultrathin
620 carbon (LFH7100AR35, Electron Microscopy Sciences). After 2.5 min incubation inside
621 the Vitrobot chamber, the excess solution was manually blotted and a fresh sample of 3.5
622 µl was reapplied inside the Vitrobot chamber and incubated for another 2.5 min. For the
623 Dhr1 and Kre33 dataset, a total of five applications were done on each grid. The grid was
624 then blotted (blot force of 8 and blot time of 9 s) and plunged into liquid ethane. For the
625 Dhr1dataset, a total of two applications were done for each grid. The grid was then blotted
626 (blot force of 8 and blot time of 7 s) and plunged into liquid ethane and for the Dhr1 and
627 Utp14 dataset, a total of five applications were done on each grid to achieve a good

628 distribution of particles. The grid was then blotted (blot force of 8 and blot time of 9 s) and
629 plunged into liquid ethane. Grids were imaged on a Titan Krios electron microscope (FEI)
630 with an energy filter (slit width of 20 eV) and a K3 Summit detector (Gatan) operating at
631 300 kV with a nominal magnification of ×64,000.

632 SerialEM[30] was used to collect four datasets. 44,272 micrographs were collected
633 for the Kre33/Dhr1 dataset, two datasets of Dhr1 were collected totaling to 84,463
634 micrographs and 85,031 micrographs were collected for Dhr1 and Utp14 dataset. All
635 datasets were collected with a defocus range of −1 to −2.5 µm and a super-resolution
636 pixel size of 0.54 Å. Micrographs contained 40 frames using a total dose of 25.3-
637 30.8 e−per pixel per second (specimen pixel size of 1.08 Å per pixel) with an exposure
638 time of 2-2.5 s and a total dose of 61.7 -63.1e− Å−2. A multi-shot strategy was used to
639 record nine micrographs per hole at each stage position with the same defocus range,
640 electron dose and frame count.

641

642 **Cryo-EM data processing Dhr1 and Kre33 dataset**

643 The Dhr1 and Kre33 dataset was processed using a combination of RELION
644 5beta[31] and cryoSparc v4.6[ref32]. 44,272 movies were gain corrected, dose weighted,
645 aligned, with each dataset having different optic groups and binned to a pixel size of 1.08
646 Å using RELION's implementation of a MotionCor2-like algorithm[33]. Micrograph defocus
647 was estimated using Gctf[34] . Particles were picked using Laplacian (autopick) in RELION
648 5beta and post 2D classification a total of 2,817,609 particles were re-extracted at a pixel
649 size of 4.32 Å per pixel (4× binning) and underwent 3D classification in RELION 5beta
650 with alignment using a reference map from previous datasets. Two good classes were

651 combined, and duplicates were removed to result in 308,351 total particles. These
652 particles were subjected to three rounds of CTF refinement and Bayesian polishing in
653 RELION 5beta. Post polishing all homogenous refinements were completed in CryoSparc
654 v4.6 and classifications were all done in RELION 5beta, particle positions from cryosparc
655 are converted into RELION using pyem software csparc2star.py[35] . The polished particles
656 were subjected to a homogenous refinements resulting in a reconstruction at a global
657 resolution of 3.3 Å. To separate the states present in the consensus reconstruction,
658 multiple 3D classifications without alignment were performed. This was followed by 3D
659 variability[36] in CryoSparc v4.6 for analysis of the type of heterogeneity present in the data
660 which guided the creation of a mask around the region of interest and further 3D
661 classification without alignment on the region of variability. Eight distinct states (sates A-
662 G) were isolated from the dataset that showed unique features in the progression of
663 maturation of the SSU processome pathway (**Supplementary Fig.1**). The global
664 resolution of the eight states ranged from 3-5.9 Å.
665

666 **Cryo-EM data processing Dhr1 dataset**

667 Dhr1 dataset was processed using a combination of RELION 5beta[31] and
668 cryoSparc v4.6[ref32] . 84,463 movies were gain corrected, dose weighted, aligned, with
669 each dataset having different optic groups and binned to a pixel size of 1.08 Å using
670 RELION's implementation of a MotionCor2-like algorithm[33] . Micrograph defocus was
671 estimated using Gctf[34] . Particles were picked using crYOLO 1.7.5[37] and post 2D
672 classification a total of 13,198,550 particles were re-extracted at a pixel size of 4.32 Å per
673 pixel (4× binning) and underwent heterogenous refinement in CryoSparc v4.6 using a

674 reference map from previous classification in RELION 5beta. One good class was
675 isolated resulting in 1,933,969 total particles. These particles were subjected to three
676 rounds of CTF refinement and Bayesian polishing in RELION 5beta. Post polishing all
677 homogenous refinements were completed in CryoSparc v4.6 and classifications were all
678 done in RELION 5beta. Particle positions from cryosparc are converted into RELION
679 using pyem software csparc2star.py[35] . The polished particles were subjected to a
680 homogenous refinement resulting in a reconstruction at a global resolution of 3 Å. To
681 separate the states present in the consensus reconstruction, multiple iterations of 3D
682 classifications without alignment was performed. Followed by 3D variability[36] in
683 CryoSparc v4.6 for analysis of the type of heterogeneity present in the data which guided
684 the creation of a mask around the region of interest and further 3D classification without
685 alignment on the region of variability. Seven distinct states (sates H-N) were isolated from
686 the dataset that showed unique features in the progression of the disassembly of the SSU
687 processome pathway (**Supplementary Fig.2**). The global resolution of the seven states
688 ranged from 2.65-4.3 Å.
689

690 **Cryo-EM data processing Dhr1 and Utp14 dataset**

691 The Dhr1 and Utp14 dataset was processed using a combination of RELION
692 5beta[31] and cryoSparc v4.6[ref32] . 85,031 movies were gain corrected, dose weighted,
693 aligned, with each dataset having different optic groups and binned to a pixel size of 1.08
694 Å using CryoSparc v 4.6 motion correction. Micrograph defocus was estimated using
695 Patch CTF and particles were picked using a template picker resulting in a total of
696 27,069,273 particles which underwent heterogenous refinement and subsequent global

697 and local CTF refinements, followed by reference motion correction. Post polishing all
698 homogenous refinements were completed in CryoSparc v4.6 and classifications were all
699 done in RELION 5beta. Particle positions from cryosparc are converted into RELION
700 using pyem software csparc2star.py[35] . The polished particles were subjected to a
701 homogenous refinement resulting in a reconstruction at a global resolution of 2.9 Å. To
702 separate the states present in the consensus reconstruction, multiple iterations of 3D
703 classifications without alignment were performed. Followed by 3D variability[36] in
704 CryoSparc v4.6 for analysis of the type of heterogeneity present in the data which guided
705 the creation of a mask around the region of interest and further 3D classification without
706 alignment on the region of variability. State O was isolated from the dataset with global
707 resolution of 3.25 Å that showed clear density for Utp14-bound Dhr1 (**Supplementary**
708 **Fig. 3**).
709
710 **Generation of focused and composite maps for model buildings**
711 Composite maps for the total of 16 states were generated from combined focused
712 maps to facilitate model building. Focused maps were generated using subtraction and
713 refinement masks generated in CryoSparc v4.6. Each focused map was made by particle
714 subtraction with a masked region followed by masked local refinement. Local resolution
715 estimation for overall and all focused maps and filtering of the overall map were performed
716 using CryoSparc v4.6. Focused maps were combined into a composite map using the
717 'vop max' command in ChimeraX[38] (**Supplementary Figs. 4-25**).
718
719

720 **Model building and refinement**

721 A combination of AlphaFold structure predictions[39] , existing X-ray/EM structures,
722 and *de novo* model building was used to build the 16 SSU processome assembly
723 intermediates. A starting model (PDB: 5WLC/6KE6) that included all ribosomal proteins
724 and RNA was used as initial template for rigid body docking into the State H composite
725 map since it is of highest resolution. All template ribosomal protein models were manually
726 adjusted using COOT[40] . State H was then used as a template to build the proteins and
727 RNA into the other 15 states with manual adjustments in COOT. The final models for the
728 16 states were real-space refined with three cycles of refinement in PHENIX using
729 phenix.real_space_refine[41] using secondary structure restraints for proteins and RNA. In
730 regions with medium to low resolution, protein sidechains were trimmed to the C_β position
731 after all-atom refinement. The final model refinement statistics can be found in
732 **Supplementary Table 1**. The maps and models were analyzed and visualized in
733 ChimeraX[38] .

734

735 **SSU processome predictome**

736 Proteins present within States A-O together with 14 exosome proteins were screened for
737 binary interactions. The resulting 3570 unique interactions were screened using the
738 default settings in the AlphaPulldown[23] implementation of Alphafold-Multimer[22]. For the
739 SSU processome predictome (**Fig. 2a**) the median iptm_ptm score of five models was
740 plotted (**Extended Data Table 2**).

741

742

743

744 **Yeast Growth Assays**

745 The *rrp6Δ utp14 Δ* strain and *rrp6Δ utp18 Δ utp14 Δ* strain in the BY4741
746 background were used for all studies. These strains were transformed with two yeast
747 centromeric vectors, one vector under URA3 selection bearing wild-type RRP6 and
748 UTP14 derived from pRSII416 and second vector under LEU2 selection bearing wild-type
749 RRP6 or rrp6 alleles containing mutations or c-terminal truncations in conjunction with
750 UTP14 wild-type or utp14 alleles containing mutations derived from pRSII415. Strains
751 carrying both pRSII415 and pRSII416 plasmids were selected on minimal media (SD-Ura
752 and Leu) after transformation. Colonies grown on the selection plates were selected and
753 grown in minimal media (SD-Ura and Leu) liquid cultures. Loss of the *URA3* plasmid was
754 done on minimal media agar plates (SD–Leu + 5-FOA) plates by spotting serial 10-fold
755 dilutions (starting at OD_{600} of 1) of liquid cultures. Growth was monitored at 30°C over a
756 period of 5 days.

757

758 **Data availability**

759 Raw unaligned multi-frame movies and aligned micrographs have been deposited in the
760 Electron Microscopy Public Image Archive: Dhr1 and Kre33 dataset: EMPIAR-XXXX,
761 Dhr1 dataset: EMPIAR-XXXX, and Dhr1 and Utp14 dataset: EMPIAR-XXXX. The cryo-
762 EM maps and atomic models have been deposited in the Electron Microscopy Data Bank
763 (EMDB) and the Protein Data Bank (PDB): State A (EMDB-49075, PDB 9N6V), State A*
764 (EMD-49076, PDB 9N6W), State B (EMD-49077, PDB 9N6X), State C (EMD-49078, PDB
765 9N6Y), Sate D (EMD-49079, PDB 9N6Z), Sate E (EMD-49080, PDB 9N70), State F

766 (EMD-49082, PDB 9N72), State G (EMD-49083, PDB 9N73), State H (EMD-49084, PDB
767 9N74), State I (EMD-49085, PDB 9N75), State J (EMD-49086, PDB 9N76), State K
768 (EMD-49087, PDB 9N77), State L (EMD-49088, PDB 9N78), State M (EMD-49089, PDB
769 9N79), State N (EMD-49090, PDB 9N7A), State O (EMD-49091, PDB 9N7B).
770

771 **Acknowledgements**
772 We would like to thank M. Ebrahim, J. Sotiris, and H. Ng at the Evelyn Gruss Lipper Cryo-
773 Electron Microscopy Resource Center at The Rockefeller University for assistance with
774 grid screening and data collection. Mass spectrometry data was generated by the
775 Proteomics Resource Center at The Rockefeller University (RRID:SCR_017797) using
776 instrumentation funded by the Sohn Conferences Foundation and the Loena M. and Harry
777 B. Helmsley Charitable Trust, and we particularly thank H. Molina, S. Heissel, and C.
778 Peralta for assistance. We thank A. Vanden Broeck for advice with cryo-EM data
779 processing and scripts for figures. We also thank K. Ye for sharing experimental data from
780 a prior study[10] and members of the Klinge laboratory for critical reading of this manuscript.
781

782 **Author information**
783 Laboratory of Protein and Nucleic Acid Chemistry, The Rockefeller University, New York,
784 NY, USA
785 Sebastian Klinge, Olga Buzovetsky
786
787
788

789

790 **Contributions**

791 S.K. conceived the study. O.B. and S.K. designed the experiments and analyzed data.
792 O.B. performed all experiments, including strain generation, complex purification, cryo-
793 EM data processing, model building, and yeast genetics studies. All authors wrote and
794 edited the manuscript.

795

796 **Corresponding author**

797 Correspondence to Sebastian Klinge (klinge@rockefeller.edu).

798

799 **Ethics declarations**

800 The authors declare no competing interests.

801

802 **Funding**

803 Research reported in this publication was supported by the National Institute of General
804 Medical Sciences of the National Institutes of Health under Award Numbers
805 R01GM145950 and R35GM156426, and the Chan Zuckerberg Initiative Exploratory Cell
806 Network.

807

808 **Supplementary Information.** Supplementary Figs. 1-28

809 **Extended Data.** Extended Data Figs. 1-6, Extended Data Tables 1 and 2.

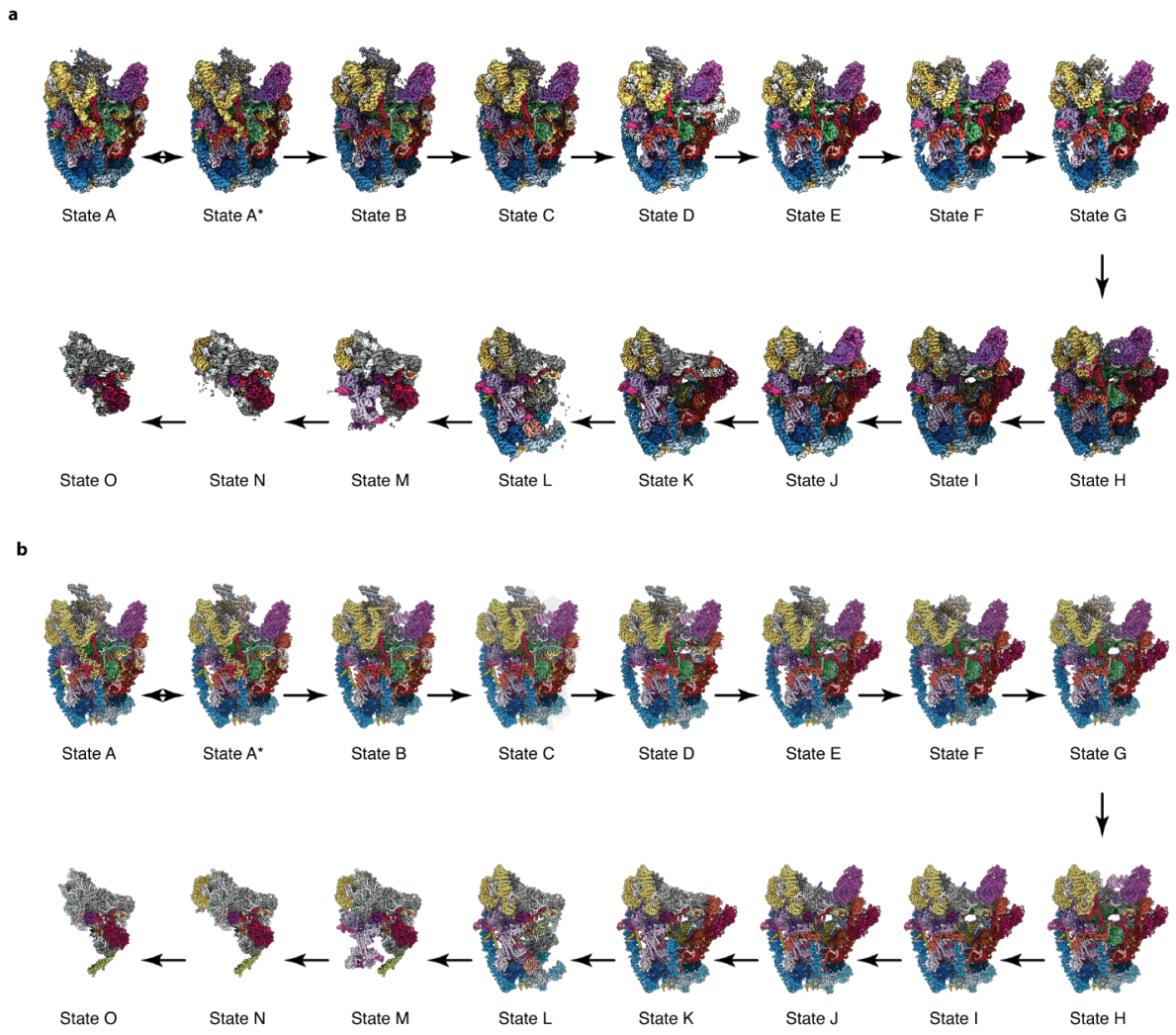

Extended Data Fig. 1. Cryo-EM maps and models of the SSU processomes. (**a**) Composite cryo-EM maps and (**b**) atomic models colored by protein components highlighting stepwise maturation of the SSU processome.

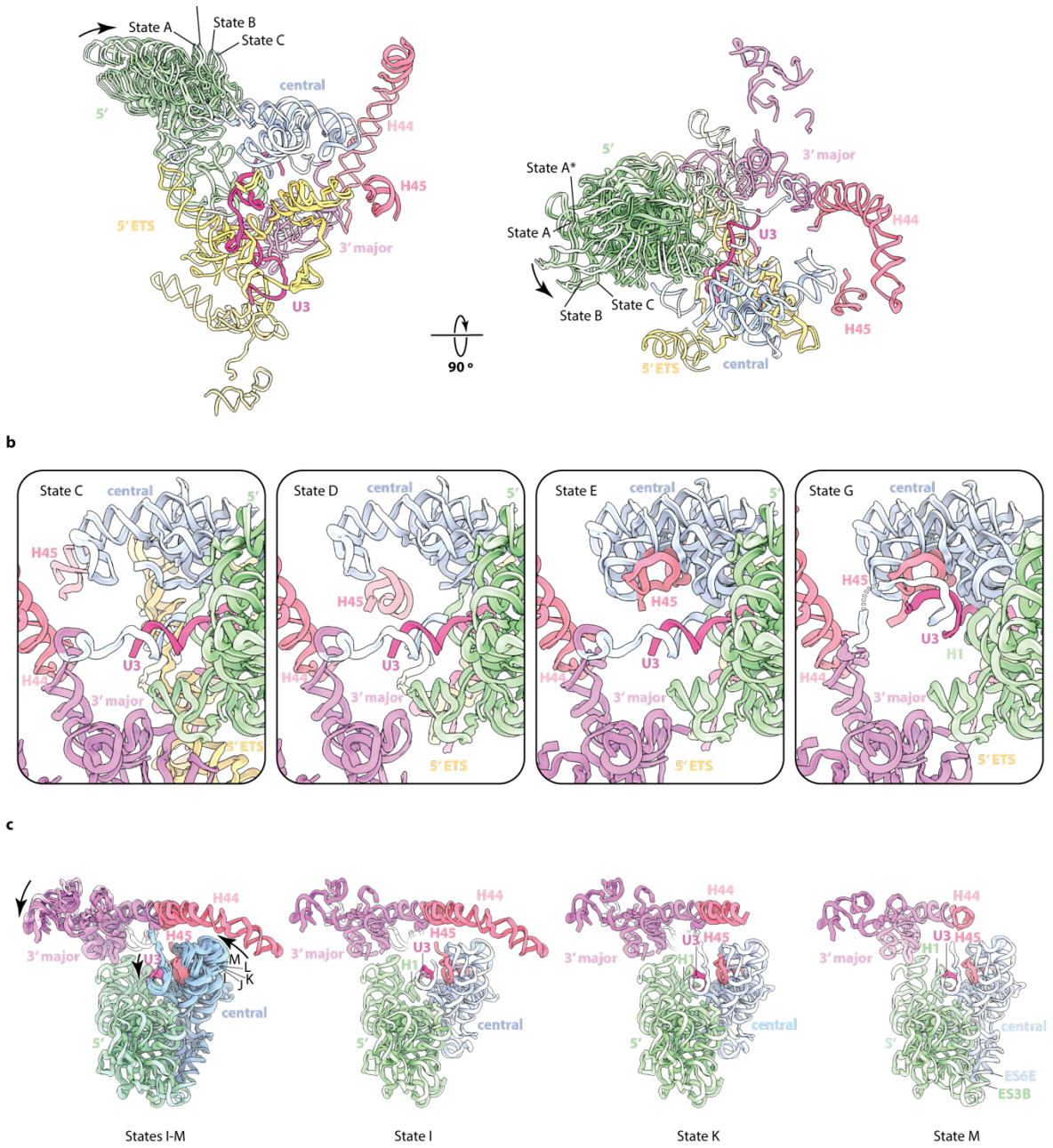

Extended Data Fig. 2. rRNA compaction and folding events across states.

(**a**) Compaction of the 18*S* 5′ domain from States A-C side view (left) and top view (right). Labeled RNA elements are color coded. Arrows highlight compaction between states A

818 and C. (**b**) Simplified rRNA folding events leading up to A1 cleavage. (**c**) Compaction of

819 the central and 5′ domains during states I-M.

820

821

822

823

824

825

826

827

828

829

830

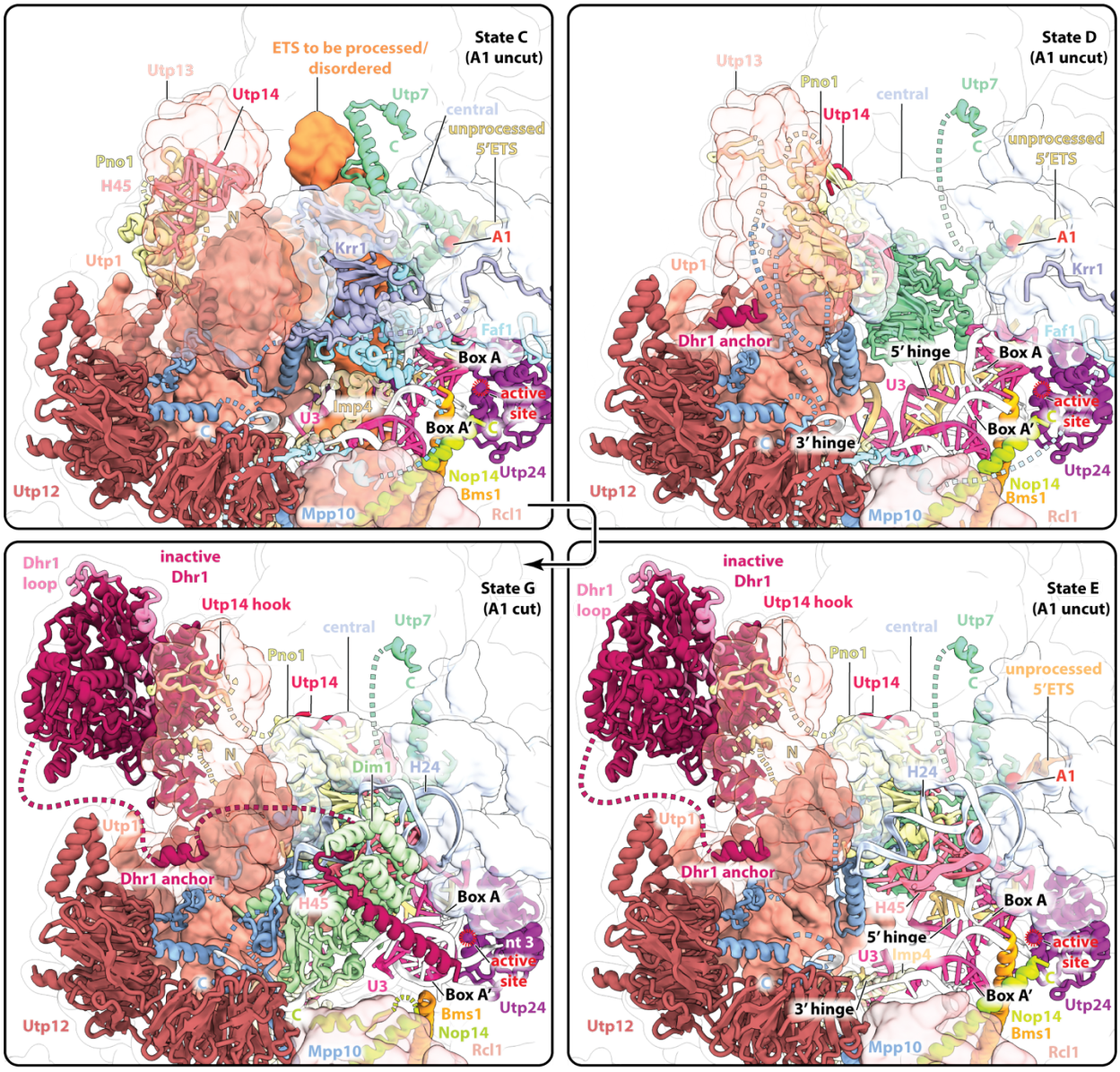

Extended Data Fig. 3. Molecular proofreading for A1 cleavage during SSU processome maturation. Detailed views involving states prior to (States C, D, E) and after A1 cleavage (State G) with color-coded proteins. The A1 cleavage site, U3 architectural sites, and active site of Utp24 are highlighted and flexible interactions indicated by dashed lines.

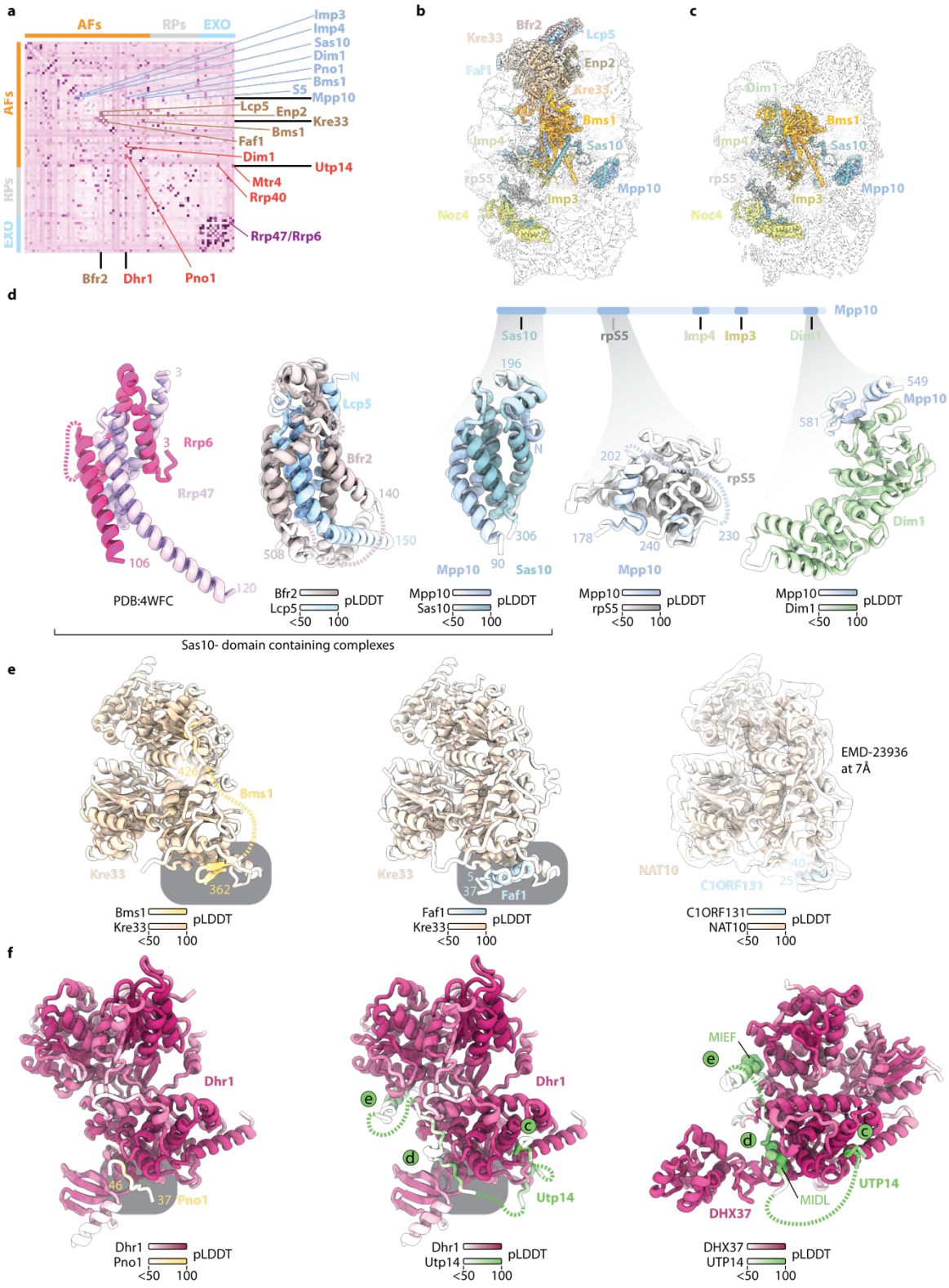

838

839 **Extended Data Fig. 4. Yeast SSU processome predictome.**

840 (**a**) Color coded yeast SSU processome predictome between assembly factors (AFs),
841 ribosomal proteins (RPs) and RNA exosome proteins (EXO). Key interactors of Mpp10,
842 Kre33, Utp14, Dhr1 and Bfr2 are color coded. (**b**) State C containing proteins listed in (a).
843 (**c**) State H containing proteins listed in (a). (**d**) Sas10-domain containing Rrp6/Rrp47
844 complex and predicted Bfr2-Lcp5, and Mpp10-Sas10 complexes. The schematic of
845 Mpp10 contextualizes predictions of Mpp10 interactors. (**e**) Mutually exclusive
846 interactions with Kre33 (human NAT10) predicted for Bms1 and Faf1 (human C1orf131).
847 (**f**) Predictions of Dhr1/DHX37 interactions. Mutually exclusive binding of Pno1 and Utp14
848 to yeast Dhr1 are highlighted. Elements of human UTP14 known to activate human
849 DHX37 (MIDL, MIEF)[19] are indicated. Confidence levels (pLDDT) are color coded for
850 each protein.
851
852

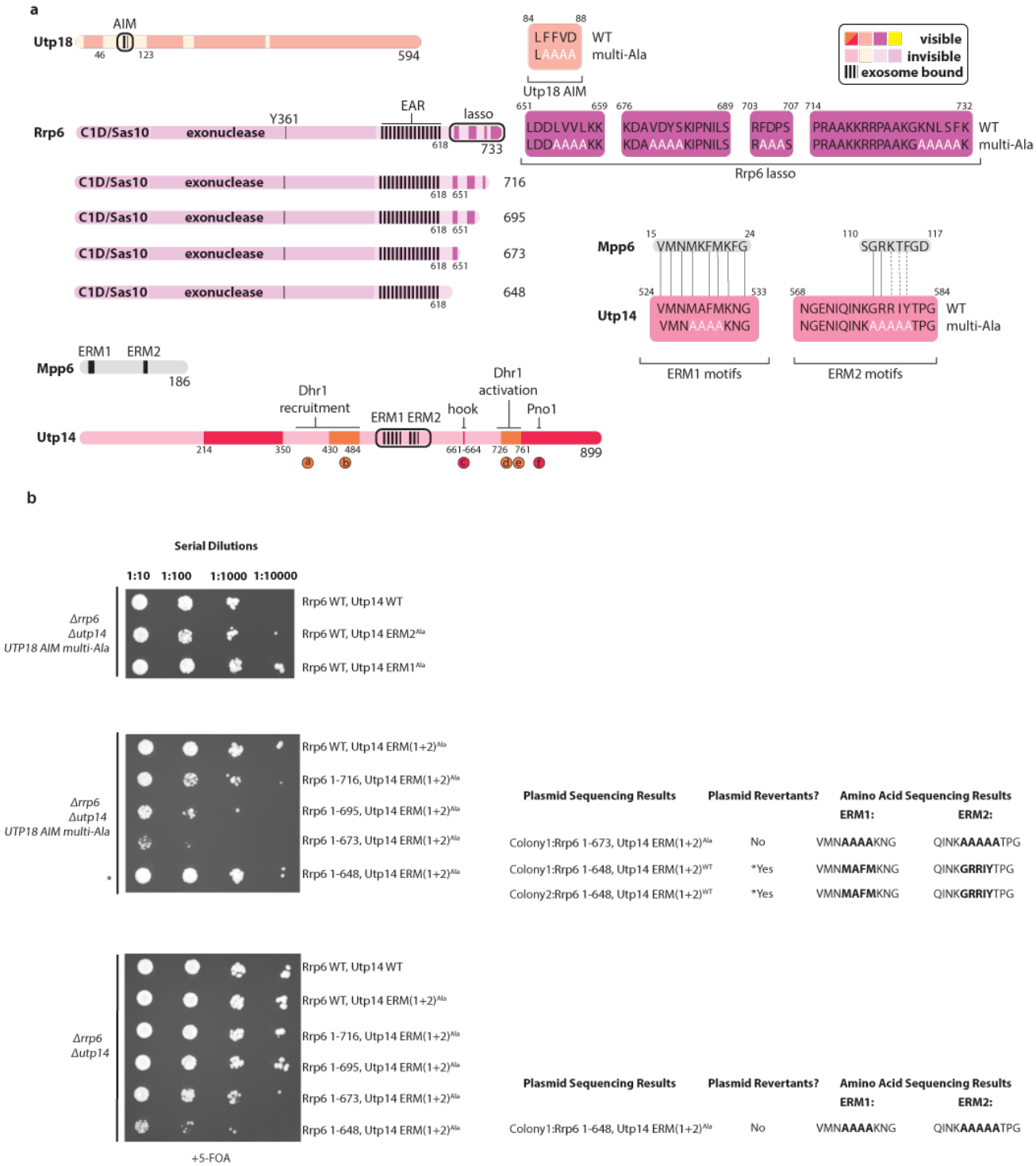

Plasmid Sequencing Results	Plasmid Revertants?	Amino Acid Sequencing Results ERM1:	ERM2:
Colony1:Rrp6 1-673, Utp14 ERM(1+2)^{Ala}	No	VMN**AAAA**KNG	QINK**AAAAA**TPG
Colony1:Rrp6 1-648, Utp14 ERM(1+2)^{WT}	*Yes	VMN**MAFM**KNG	QINK**GRRIY**TPG
Colony2:Rrp6 1-648, Utp14 ERM(1+2)^{WT}	*Yes	VMN**MAFM**KNG	QINK**GRRIY**TPG

Plasmid Sequencing Results	Plasmid Revertants?	Amino Acid Sequencing Results ERM1:	ERM2:
Colony1:Rrp6 1-648, Utp14 ERM(1+2)^{Ala}	No	VMN**AAAA**KNG	QINK**AAAAA**TPG

853

854 **Extended Data Fig. 5. Yeast growth assays.**

855 (**a**) Schematics of Utp18, Rrp6, Mpp6, and Utp14 with interacting and functional elements
856 labeled with multi-Ala mutations used in this study as well as an alignment to Mpp6
857 exosome recruitment motif, indicated in grey. Designed truncations of Rrp6 lasso (bottom
858 left) with interacting and functional elements labeled. Locations of all alanine substitutions
859 for Utp18, Rrp6, and Utp14 are indicated on the right. (**b**) Growth analysis of Utp18 multi-
860 Ala mutant in Δrrp6 and Δutp14 background (top and middle panels) and Utp18 WT in
861 Δrrp6 and Δutp14 background (bottom panel). Growth assay using WT, truncations and
862 mutant Rrp6 or Utp14 constructs in the absence of genomic Rrp6 and Utp14. Colonies
863 sequenced are indicated on the right of the growth assays.
864
865
866
867
868
869
870
871
872
873
874
875
876
877

878

879

880

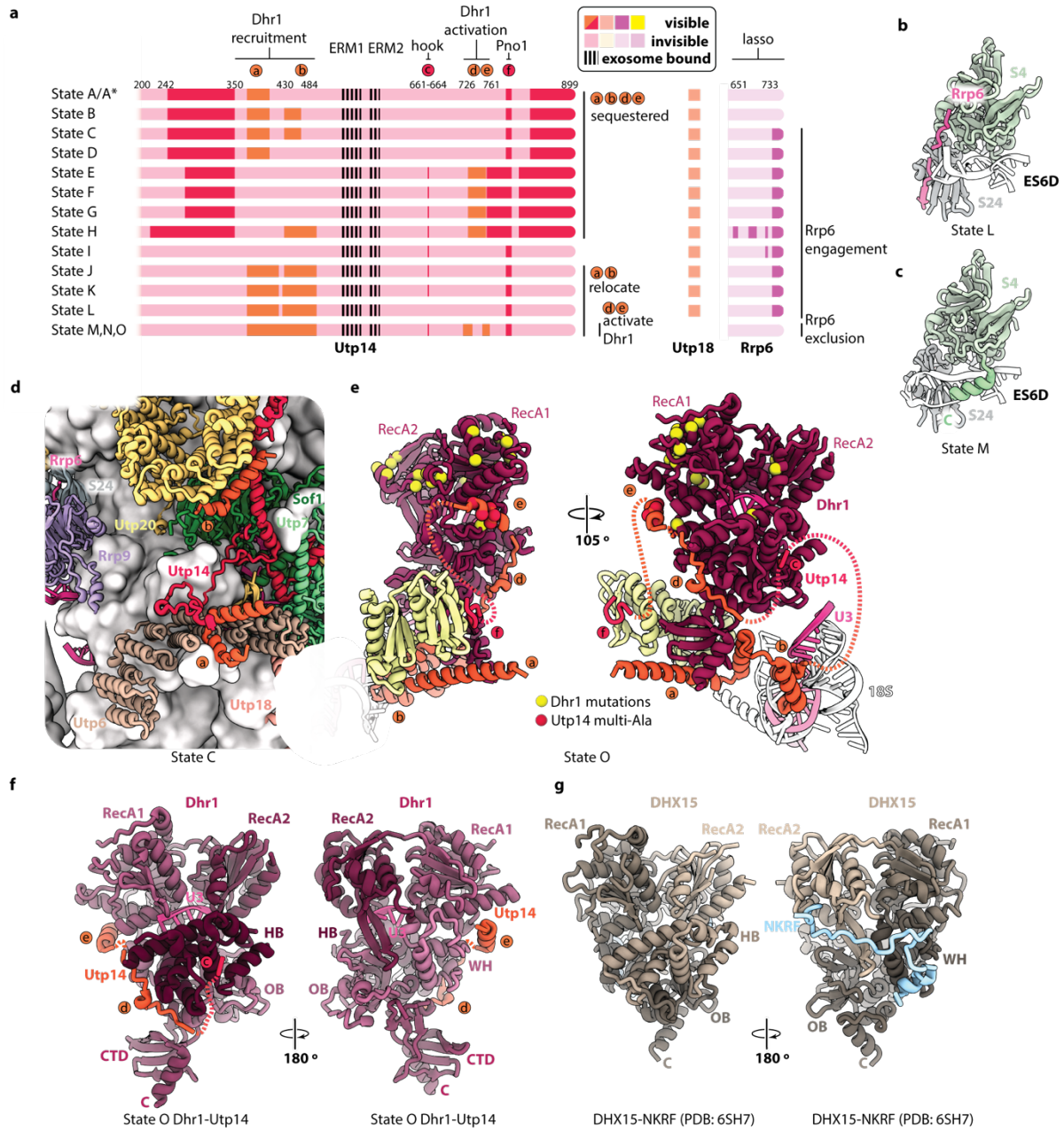

881

882 **Extended Data Fig. 6. Functional elements of Utp14, Rrp6, Utp18 and Dhr1.**

883 (**a**) Schematics of Utp14, Utp18 and Rrp6 across States A-O. Utp14 functional sequence
884 elements structured, bound, relocated, or activating are indicated on the left and the
885 presence/absence of Utp18 is indicated in the middle. Visible regions of the Rrp6 C-
886 terminus (lasso) are indicated on the right. (**b**) Binding of Rrp6 lasso to ribosomal proteins
887 S24 in State L. (**c**) Rrp6 exclusion by ES6D and S4 in State M. (**d**) State C highlights the
888 initial binding of the Rrp6 lasso and the initial sequestration of Utp14 elements a and b
889 that later recruit Dhr1. (**e**) Previously characterized mutations[18,42] mapped onto Dhr1 and
890 Utp14 represented in State O. Functional elements of Utp14 are shown in orange. (**f**)
891 Mode of Dhr1 activation by Utp14 in State O. (**g**) Mode of activation of DHX15 by G-patch
892 protein NKRF (PDB: 6SH7).
893

	State A PDB 9N6V EMD-49075	**State A*** PDB 9N6W EMD-49076	**State B** PDB 9N6X EMD-49077	**State C** PDB 9N6Y EMD-49078	**State D** PDB 9N6Z EMD-49079	**State E** PDB 9N70 EMD-49080
Data collection and processing						
Microscope	Titan Krios	Titan Krios	Titan Krios	Titan Krios	Titan Krios	Titan Krios
Voltage (keV)	300	300	300	300	300	300
Camera	K3	K3	K3	K3	K3	K3
Magnification	64,000	64,000	64,000	64,000	64,000	64,000
Pixel size at detector (Å/pixel)	1.063	1.063	1.063	1.063	1.063	1.063
Total electron exposure (e-/Å2)	60	60	60	60	60	60
Exposure rate (e-/pixel/sec)	30	30	30	30	30	30
Number of frames collected (no.)	40	40	40	40	40	40
Defocus range (μm)	-1.0 to -2.5	-1.0 to -2.5	-1.0 to -2.5	-1.0 to -2.5	-1.0 to -2.5	-1.0 to -2.5
Energy filter slit width (V)	20	20	20	20	20	20
Automation software	SerialEM	SerialEM	SerialEM	SerialEM	SerialEM	SerialEM
Micrographs collected (no.)	44,272	44,272	44,272	44,272	44,272	44,272
Total extracted particles (no.)	2,817,609	2,817,609	2,817,609	2,817,609	2,817,609	2,817,609
Final particle images (no.)	36,965	56,168	28,151	23,899	12,826	9,125
Point-group symmetry	C1	C1	C1	C1	C1	C1
Resolution (global at FSC-0.143, Å)						
Overall map (masked)	3.23	3.05	3.71	3.65	4.74	5.17
Map sharpening *B* factor ($Å^2$)						
Overall map	-26.2	-35.8	-28.9	-23.3	-21.5	-32.6
Focused maps	-26.2 to -583.3	-35.8 to -423.3	-26.2 to -88.6	-23.3 to -80	-4.8 to -297.7	-20.6 to -241.1
Model composition						
Non-hydrogen atoms	243,904	243,904	244,461	245,176	157,426	162,545
Chains (proteins/RNA)	73/3	73/3	73/3	74/3	68/3	69/3
Protein residues	26,535	26,535	26,820	26,828	25,260	26,098
RNA residues	1847	1847	1825	1825	1430	1471
Ligands (Mg^{2+}/Zn^{2+}/ ATP/ADP/GTP)	25/2/1/0/ 1/	25/2/1/0/ 1/	34/2/1/0/ 1/	34/2/1/0/ 1/	0/0/0/0/ 0/	0/0/0/0/ 0/
Model refinement						
Refinement package (real space)	Phenix 1.19.1	Phenix 1.19.1	Phenix 1.19.1	Phenix 1.19.1	Phenix 1.19.1	Phenix 1.19.1
Initial models used (PDB code)	9N6W	9N74	9N6W/9N74	9N6W/9N74	9N6W/9N74	9N6W/9N74
Model resolution cutoff (Å)	3.4	3.3	3.9	3.9	5.0	6.5
Model-Map CC (CC_{mask}/CC_{box}/ CC_{peaks}/CC_{volume})	0.77/0.76/ 0.68/0.77	0.79/0.76/ 0.71/0.78	0.76/0.74/ 0.65/0.76	0.77/0.76/ 0.67/0.77	0.66/0.76/ 0.50/0.66	0.69/0.76/ 0.56/0.69
Model-to-map FSC, threshold 0.50 (masked/unmasked, Å)	3.27/3.51	3.13/3.31	3.87/4.06	3.81/4.04	6.90/7.59	6.73/7.52
RMSDs						
Bond lengths (Å)	0.004	0.004	0.005	0.004	0.004	0.004
Bond angles (°)	0.890	0.912	0.955	0.923	1.021	1.028
B-factors						
Average B-factors (A^2)						
Protein	88.75	62.35	90.82	95.63	257.44	229.78
RNA	111.41	87.92	109.42	109.97	281.97	263.75
Ligand	75.43	57.49	67.50	73.12	-	-
Validation						
Clash score	3.60	3.47	5.21	4.50	1.37	1.36
MolProbity score	1.15	1.14	1.30	1.22	0.87	0.87
CaBLAM outliers	3.11	3.02	3.33	3.14	3.27	3.20
Poor rotamers (%)	0.00	0.00	0.01	0.00	0.00	0.00
C-beta deviations	0.00	0.00	0.00	0.00	0.00	0.02
EMRinger score	2.49	2.95	1.98	2.13	N/A	N/A
Ramachandran plot						
Favored (%)	98.54	98.38	97.91	98.30	98.01	98.14
Allowed (%)	1.46	1.62	2.09	1.70	1.99	1.86
Outliers (%)	0.00	0.00	0.00	0.00	0.00	0.00
RNA validation						
Average suiteness (%)	58.3	57.9	54.4	55.6	54.1	52.7
Good sugar puckers (%)	99.94	99.94	99.95	99.89	99.93	99.72

	State F PDB 9N72 EMD-49082	**State G** PDB 9N73 EMD-49083	**State H** PDB 9N74 EMD-49084	**State I** PDB 9N75 EMD-49085	**State J** PDB 9N76 EMD-49086	**State K** PDB 9N77 EMD-49087
Data collection and processing						
Microscope	Titan Krios	Titan Krios	Titan Krios	Titan Krios	Titan Krios	Titan Krios
Voltage (keV)	300	300	300	300	300	300
Camera	K3	K3	K3	K3	K3	K3
Magnification	64,000	64,000	64,000	64,000	64,000	64,000
Pixel size at detector (Å/pixel)	1.063	1.063	1.063	1.063	1.063	1.063
Total electron exposure (e-/Å2)	60	60	61.6	61.6	61.6	61.6
Exposure rate (e-/pixel/sec)	30	30	30.8	30.8	30.8	30.8
Number of frames collected (no.)	40	40	40	40	40	40
Defocus range (μm)	-1.0 to -2.5	-1.0 to -2.5	-1.0 to -2.5	-1.0 to -2.5	-1.0 to -2.5	-1.0 to -2.5
Energy filter slit width (V)	20	20	20	20	20	20
Automation software	SerialEM	SerialEM	SerialEM	SerialEM	SerialEM	SerialEM
Micrographs collected (no.)	44,272	44,272	84,463	84,463	84,463	84,463
Total extracted particles (no.)	2,817,609	2,817,609	13,198,550	13,198,550	13,198,550	13,198,550
Final particle images (no.)	6,227	4,987	328,554	95,512	11,394	19,571
Point-group symmetry	C1	C1	C1	C1	C1	C1
Resolution (global at FSC-0.143, Å)						
Overall map (masked)	5.94	5.96	2.69	3.01	4.23	3.94
Map sharpening *B* factor ($Å^2$)						
Overall map	-88.2	-72.7	-65.4	-45.5	-11.6	-16
Focused maps	-17.9 to -529.7	-12.7 to -309.5	-65.3 to -86.7	-51.5 to -79.5	-116 to -29.9	-16 to -40.2
Model composition						
Non-hydrogen atoms	162,433	163,806	238,225	220,521	206,690	190,271
Chains (proteins/RNA)	70/3	71/3	75/3	72/3	70/3	66/3
Protein residues	25,995	26,337	25,221	23,094	23,115	21,392
RNA residues	1491	1474	1761	1710	1722	1661
Ligands (Mg^{2+}/Zn^{2+}/ ATP/ADP/GTP)	0/0/0/0/ 0	0/0/0/0/ 0	39/3/1/1/ 1	59/3/1/1/ 1	38/2/1/1/ 1	48/2/0/1/ 1
Model refinement						
Refinement package (real space)	Phenix 1.19.1	Phenix 1.19.1	Phenix 1.19.1	Phenix 1.19.1	Phenix 1.19.1	Phenix 1.19.1
Initial models used (PDB code)	9N6W/9N74	9N6W/9N74	5WLC/6KE6	9N74	9N75	9N76
Model resolution cutoff (Å)	6.5	6.5	3.0	3.3	4.5	4.2
Model-Map CC (CC_{mask}/CC_{box}/ CC_{peaks}/CC_{volume})	0.63/0.74/ 0.49/0.64	0.68/0.76/ 0.52/0.67	0.77/0.77/ 0.74/0.78	0.77/0.77/ 0.72/0.77	0.73/0.75/ 0.60/0.72	0.74/0.76/ 0.64/0.74
Model-to-map FSC, threshold 0.50 (masked/unmasked, Å)	7.51/8.02	7.30/7.84	2.84/2.99	3.14/3.29	4.37/6.33	4.09/4.50
RMSDs						
Bond lengths (Å)	0.005	0.004	0.005	0.004	0.004	0.004
Bond angles (°)	1.023	1.025	0.919	0.895	0.947	0.930
B-factors						
Average B-factors (A^2)						
Protein	223.98	226.01	29.43	48.61	152.23	118.18
RNA	250.68	248.95	39.81	64.27	176.40	141.33
Ligand	-	-	32.71	52.81	155.15	111.32
Validation						
Clash score	3.67	1.07	3.39	3.22	5.79	4.94
MolProbity score	1.16	0.81	1.13	1.11	1.32	1.26
CaBLAM outliers (%)	3.33	3.29	3.13	3.07	3.17	3.29
Poor rotamers (%)	0.00	0.00	0.00	0.01	0.05	0.05
C-beta deviations	0.00	0.00	0.00	0.00	0.01	0.00
EMRinger score	N/A	N/A	3.54	2.76	0.64	1.17
Ramachandran plot						
Favored (%)	98.13	98.07	98.42	98.57	98.34	98.23
Allowed (%)	1.87	1.93	1.58	1.43	1.66	1.77
Outliers (%)	0.00	0.00	0.00	0.00	0.00	0.00
RNA validation						
Average suiteness (%)	51.8	53.4	54.0	56.2	55.3	54.9
Good sugar puckers (%)	99.66	99.59	99.54	99.46	99.36	99.34

	State L	State M	State N	State O
	PDB 9N78 EMD-49088	PDB 9N79 EMD-49089	PDB 9N7A EMD-49090	PDB 9N7B EMD-49091
Data collection and processing				
Microscope	Titan Krios	Titan Krios	Titan Krios	Titan Krios
Voltage (keV)	300	300	300	300
Camera	K3	K3	K3	K3
Magnification	64,000	64,000	64,000	64,000
Pixel size at detector (Å/pixel)	1.063	1.063	1.063	1.063
Total electron exposure (e-/Å2)	61.6	61.6	61.6	61.6
Exposure rate (e-/pixel/sec)	30.8	30.8	30.8	30.8
Number of frames collected (no.)	40	40	40	40
Defocus range (μm)	-1.0 to -2.5	-1.0 to -2.5	-1.0 to -2.5	-1.0 to -2.5
Energy filter slit width (V)	20	20	20	20
Automation software	SerialEM	SerialEM	SerialEM	SerialEM
Micrographs collected (no.)	84,463	84,463	84,463	85,031
Total extracted particles (no.)	13,198,550	13,198,550	13,198,550	27,069,273
Final particle images (no.)	10,725	12,127	14,551	131,106
Point-group symmetry	C1	C1	C1	C1
Resolution (global at FSC-0.143, Å)				
Overall map (masked)	4.17	3.93	3.84	3.25
Map sharpening *B* factor ($Å^2$)				
Overall map	-12.2	-16.6	-20.2	-52.4
Focused maps	-12.2 to -30.9	-24.4 to -90.2	-27.9 to -78.8	-60.3 to -85.2
Model composition				
Non-hydrogen atoms	149,183	106,665	93,089	85,883
Chains (proteins/RNA)	60/3	46/3	40/3	38/3
Protein residues	15,942	10,667	8,701	7,602
RNA residues	1587	1493	1428	1428
Ligands (Mg^{2+}/Zn^{2+}/ATP/ADP/GTP)	47/2/0/0/1	47/2/0/0/1	47/2/0/0/1	47/2/0/0/1
Model refinement				
Refinement package (real space)	Phenix 1.19.1	Phenix 1.19.1	Phenix 1.19.1	Phenix 1.19.1
Initial models used (PDB code)	9N77	9N78	9N79	9N7A
Model resolution cutoff (Å)	4.4	4.1	4.1	3.6
Model-Map CC (CC_{mask}/CC_{box}/CC_{peaks}/CC_{volume})	0.73/0.74/0.59/0.72	0.78/0.77/0.67/0.78	0.81/0.78/0.70/0.81	0.74/0.78/0.69/0.74
Model-to-map FSC, threshold 0.50 (masked/unmasked, Å)	4.17/4.83	4.07 /4.62	3.80 /4.66	3.41 /3.73
RMSDs				
Bond lengths (Å)	0.004	0.004	0.004	0.004
Bond angles (°)	0.925	0.895	0.876	0.855
B-factors				
Average B-factors (A^2)				
Protein	144.24	190.48	149.72	61.64
RNA	150.59	158.59	131.07	85.04
Ligand	86.60	103.26	85.63	38.04
Validation				
Clash score	5.08	4.15	4.07	2.99
MolProbity score	1.27	1.20	1.19	1.09
CaBLAM outliers	3.10	2.89	3.20	3.23
Poor rotamers (%)	0.05	0.05	0.04	0.00
C-beta deviations	0.00	0.00	0.00	0.00
EMRinger score	1.08	1.46	1.79	2.33
Ramachandran plot				
Favored (%)	98.30	98.48	98.37	98.28
Allowed (%)	1.70	1.52	1.63	1.72
Outliers (%)	0.01	0.00	0.00	0.00
RNA validation				
Average suiteness (%)	55.7	56.6	56.1	57.0
Good sugar puckers (%)	99.31	99.40	99.37	99.37

Extended Data Table1. Cryo-EM data collection and refinement statistics.